

Core-Shell Architectured Sulfur Coated $\alpha\text{-Fe}_2\text{O}_3$ Nano-Sheet Anode for Li-Ion Battery with In-situ Active Solid Electrolyte Interfacial Layer and Li-Sulfur Energy Storage Systems

Kavibharathy Kasiviswanathan,^[a] Desai Prashant Hanamantrao,^[a] Saraswathi Ramakrishnan,^[a] Sajan Raj,^[a] Lakshmanan Kumaresan,^[a] Vivek Paulraj,^[b] Senthil Chenrayan,^[c] Baskaran Rangasamy,*^[d] and Kumaran Vediappan*^[a]

A versatile approach is achieved through the surface coating of sulfur on $\alpha\text{-Fe}_2\text{O}_3$ nanosheet by microwave treatment that inherently supports the formation of self-induced active solid electrolyte interface (SEI) layer which effectively protects the electrode surface and enhances the cyclic stability of lithium-ion battery. The present findings on a sulfur-coated $\alpha\text{-Fe}_2\text{O}_3@\text{S-2}$ core-shell structured anode demonstrates an initial specific capacity of 1194 mAh g^{-1} at a 0.1 C rate, and an average discharge capacity of 518 mAh g^{-1} over 20 cycles. Sulfur coating proves the incredible development of an active SEI layer that prevents electrolyte decomposition and the electrode persuades with stable capacity, fast rate capability and retains

excellent coulombic efficiency for 500 cycles in LIB. GITT measurements exhibit superior Li^+ ion diffusion coefficient $D_{\text{Li}^+} = 2.87 \times 10^{-10} \text{ cm}^2 \text{s}^{-1}$ at 80% SOC for the $\alpha\text{-Fe}_2\text{O}_3@\text{S-2}$ electrode. The in-depth ex-situ evaluations uncovered a fascinating self-assembled active Li_2SO_4 electrode-electrolyte interface formation in the sulfur-coated $\alpha\text{-Fe}_2\text{O}_3$ electrode that contributes interfacial kinetics. The sulfur coated $\alpha\text{-Fe}_2\text{O}_3$ electrode exhibits an exceptional high-rate performance and coulombic efficiency even in lithium-sulfur battery. This research overthrows sulfur's significance in forming an active interfacial bridging SEI layer that facilitates lithium-ion kinetics across the interface and alleviates undesirable SEI development.

Introduction

Lithium-ion batteries (LIBs) are an indispensable part of modern society that offer electrical energy for multiple applications such as eco-friendly Electrical Vehicles (EVs), electrical flight, and portable Electronic Devices (EDs) in the electronics market.^[1,2] Though the lithium-ion battery field achieved technical maturity, a few unresolved issues limit the capacity and energy density yield in the industrial market. Negative electrodes are the key materials to achieve high capacity; however, extracting capacity equivalent to theoretical values of any anode material is a challenging task. In this material race,

worldwide researchers developed several anode materials starting from carbonaceous anodes, transition metal oxides, and metallic anodes^[3] such as Sn,^[4] Ru,^[5] Si,^[6] and lithium alloys. Among the various types of anode materials, Transition Metal Oxides (TMOs) are viable substitute because of their distinctive redox conversion mechanism and the electrochemical pathway occurring below 1.5 V Vs Li^+/Li , which involves numerous chemical valence states due to their multiple electron exchanges. Consequently, they can offer significantly higher theoretical specific capacity and operating voltage, thereby increasing the energy density of LIBs than conventional graphite anode. With these objectives, TMOs such as M_xO_y ($\text{M} = \text{Ni},$ ^[7] $\text{Mn},$ ^[8] $\text{Fe},$ ^[9-11] $\text{Co},$ ^[12] and $\text{Cu},$ ^[13] etc) possessing significant theoretical capacities have been extensively studied recently. Among these TMOs utilized for LIBs, Fe_2O_3 has emerged due to its amicable higher theoretical capacity of auspicious anode material due to its high theoretical capacity of 1007 mAh g^{-1} ,^[14,15] good thermal stability, chemical compatibility, and natural abundance.^[16] Generally, the iron oxide compounds exist in various forms such as Fe_{1-x}O , Fe_2O_3 , and Fe_3O_4 due to their impressive theoretical capacity, significant iron content, and experimental oxidation potentials of around 1.8 V Vs Li^+/Li , which outperforms other TMOs (NiO_2 , Co_3O_4 , CoO etc).^[17] The Fe_2O_3 compound exhibits four different phases viz., (Hematite)- $\alpha\text{-Fe}_2\text{O}_3$, $\beta\text{-Fe}_2\text{O}_3$, (maghemite)- $\gamma\text{-Fe}_2\text{O}_3$, and $\epsilon\text{-Fe}_2\text{O}_3$.^[18] Among these phases, $\alpha\text{-Fe}_2\text{O}_3$ (Hematite) is a high stable phase of Iron oxide with a low band gap (i.e., 2.1 eV).^[19,20] Notably, the $\alpha\text{-Fe}_2\text{O}_3$ anode material has twice the density (5.0 g cm^{-3}) of traditional graphite (2.2 g cm^{-3}),^[21] resulting in a higher specific capacity and energy density in LIBs. The

[a] K. Kasiviswanathan, D. Prashant Hanamantrao, S. Ramakrishnan, S. Raj, Dr. L. Kumaresan, Dr. K. Vediappan
Electrochemical Energy Storage and Conversion Laboratory (EESCL), Department of Chemistry, Faculty of Engineering and Technology, SRM Institute of Science and Technology, Kattankulathur-603 203, Tamil Nadu, India
E-mail: kumaranv@srmit.edu.in

[b] Dr. V. Paulraj
Department of Physics and Nanotechnology, SRM Institute of Science and Technology, Kattankulathur-603 203, Tamil Nadu, India

[c] Dr. S. Chenrayan
Department of Energy Engineering, Gyeongsang National University, Jinju-si, Gyeongnam-52725, South Korea

[d] Prof. B. Rangasamy
Department of Physics, School of Mathematics and Natural Sciences, The Copperbelt University, P.O.Box 21692, Riverside, Jambo Drive, Kitwe-10101, Zambia
E-mail: baskaran.rangasamy@cbu.ac.zm

Supporting information for this article is available on the WWW under <https://doi.org/10.1002/batt.202400018>

Hematite $\alpha\text{-Fe}_2\text{O}_3$ has significantly improved suitability and environmental compatibility for LIBs due to its unique characteristics such as thermal stability, abundant, natural availability, safety, cost-effective of raw materials,^[16] environmentally benign, excellent chemical stability, high corrosion resistance, and substantial theoretical capacity based on the maximum uptake of $6\text{Li}/\text{Fe}_2\text{O}_3$ (For 6 Li^+ ion = 1007 mAh g^{-1} which is about 3 times higher than commercial LIBs).^[22-24] This reasonable high capacity corresponds to the conversion reaction mechanism of $\alpha\text{-Fe}_2\text{O}_3$ Vs Li^+/Li .^[25] Due to its excellent benefits, the $\alpha\text{-Fe}_2\text{O}_3$ electrode is widely used as a negative electrode to store alkali ions such as Li^+ , Na^+ , and K^+ .^[26]

However, there are some of the commonly encountered challenges in using metal oxides as a negative electrode for LIBs, including (Hematite)- $\alpha\text{-Fe}_2\text{O}_3$ as follows: low electronic conductivity due to its semiconducting nature of (Hematite- $\alpha\text{-Fe}_2\text{O}_3$ is a charge transfer insulator), significant volume changes in the course of Li-ion insertion/de-insertion process resulting in the poor cycling stability, particle pulverization coupled with poor electrical conductivity due to the drop down of electrical contact among the electrode particles, Initial Capacity Fading (ICF),^[27] formation of passivation layer,^[11] and sluggish Li-ion kinetics. These crucial factors lead to rapid capacity degradation and descending lifespan upon prolonged electrochemical cycling in metal oxide anodes, limiting the real-time applications of LIB systems. To tackle these challenges and to achieve higher energy density LIBs, researchers are making various strategies including (i) structural engineering, (ii) composite engineering, or surface modifications.^[28]

In order to enhance the redox kinetics of an electrode through structural aspects, the electrode materials are tailor-made into nanoparticles with various shapes, such as nanosheets,^[29] nano-spheres,^[30] nano-disks,^[31] and nano-needles.^[32] Among these particular nanostructures, the nanosheet dimensions have attracted considerable attention due to their low mass density, excellent strain accommodation, and rapid electron and ion transport in various electrodes. On the other hand, in surface modification techniques, the electrode/anode materials are usually coated with foreign materials, which could be transition metals, TMOs, carbon, metal oxides, and any element suitable for specific redox kinetics. The primary purpose of coating the electrode with external materials, such as carbon allotropes or carbon-based materials (carbon nanofibers (CNS), graphene, CNTs)^[22,33] is to improve the structural integrity and redox kinetics of working materials by alleviating SEI layer formation, particle fracture, and volume expansion. Though the carbon allotropes act as an efficient coating material to reduce the volume expansion of most of the electrode materials, during the electrochemical processes, the working potential of the anode material is found to be reduced, which causes low energy density in LiB. In this aspect, a multi-functional better coating element is needed which reduces the volume expansion, increases ionic mobility across the particles, maintains the working potential and in addition, an effective alleviation of passive SEI formation.

SEI layer formation is one of the undesirable electrode-electrolyte interfacial surface phenomena. The surface of the

electrodes tends to react quickly with the elements and free radicals of electrolytes, leading to the drastic development of an inactive SEI layer formation. Lithium-ion can easily be reduced with oxygen, nitrogen, carbon dioxide, and any of the free radicals of the decomposed electrolyte components due to its very high electropositive nature. Because of this nature, lithium-ion is captured by surface adsorbed air molecules and also the decomposed electrolyte components to form a layer of inter-metallic compounds at the electrode-electrolyte surface. The SEI layer formation leads to numerous issues, such as electrolyte decomposition, diminished electrochemical potential, capacity degradation, poor rate capability,^[34] electrical insulating, thermal runaway, aging, and safety concerns in the LIB systems, especially when LIBs are subjected to high current densities. In the context of lithiation/delithiation processes, the inactive or spent lithium ions can readily disintegrate into the electrolyte, leading to the fracturing of the SEI layer. The SEI formation develops typically during the initial cycles, leading to substantial irreversible reactions. This leads the redox operations outside the potential boundaries of the electrolyte's stability range. Additionally, the inactive or lithiated intermetallic compounds on the anode surface reduce the ionic conductivity and performance of LIBs. An efficient way to convert the unpleasant SEI layer into an active SEI layer could possibly enhance the electrochemical performance of LIBs. In this scenario, the nano-scale engineering of $\alpha\text{-Fe}_2\text{O}_3$ with suitable surface coating may drive the electrode performance and suitability in LIBs. Opting sulfur as a surface coating element is anticipated to envelop the nanosheet particle surface and serve as a medium for Li-ion mobility among the volume of electrode particles upon cycling of Li-ion cells. The sulfur coating can alter the distribution of charge with in a crystal for electrode materials, enhance ionic conductivity, and create additional sites for Li adsorption.^[35] Surface coating of electrode particles with sulfur is expected to establish an active SEI layer at the electrode-electrolyte interface due to its strong electronegative nature, which may facilitates faster Li-ion mobility during redox reactions.

This research article mainly focuses on the mitigation of Initial Capacity Fading (ICF) so that to enhance the electrochemical performance of (Hematite)- $\alpha\text{-Fe}_2\text{O}_3$ electrode through a surface coating technique. This work introduces an innovative approach for synthesizing (Hematite)- $\alpha\text{-Fe}_2\text{O}_3$ nanosheet by pechini method followed by cost-effective surface coating with 'sulfur' as core-shell structure using two distinct methods viz., physical followed by post calcination ($\alpha\text{-Fe}_2\text{O}_3@\text{S-1}$) and physical method followed by microwave-assisted ($\alpha\text{-Fe}_2\text{O}_3@\text{S-2}$) method. The rhombohedral crystal structure of the $\alpha\text{-Fe}_2\text{O}_3$ compound is confirmed by XRD analysis whereas the HR-SEM confirms the particle surface morphology. HRTEM-SAED patterns confirm the crystallographic planes and lattice distances of the $\alpha\text{-Fe}_2\text{O}_3$ compound. The XPS analysis of as-synthesized $\alpha\text{-Fe}_2\text{O}_3$ sample confirms the octahedrally coordinated Fe^{3+} ions in the hematite phase. The cyclic voltammogram analysis confirms the redox reactions attributed to the $\text{Li}_2\text{Fe}_2\text{O}_3$ followed by conversion reaction which accommodates 6 Li^+ ions in the initial cycle. However, the bare $\alpha\text{-Fe}_2\text{O}_3$ electrode entertains the passive SEI

formation while the microwave assisted sulfur coated $\alpha\text{-Fe}_2\text{O}_3$ electrode is engaged with an active Li_2SO_4 SEI layer formation which protects the electrode surface from direct exposure to the electrolyte and facilitates Li^+ ion mobility across the interface as evidenced from diffusion results. The galvanostatic results of $\alpha\text{-Fe}_2\text{O}_3@\text{S-2}$ electrode show an initial discharge capacity of 1194 mAh g^{-1} at 0.1 C-rate and the electrode delivers an excellent cycling stability for 500 cycles at 1 C. The existence of Li_2SO_4 based SEI layer on the surface of the post-redoxed sulfur coated Fe_2O_3 electrode is confirmed through detailed ex-situ HR-SEM, EDX and XRD analyses. In order to understand the versatility of the electrode, the applicability of $\alpha\text{-Fe}_2\text{O}_3@\text{S-2}$ in Li-S battery has been evaluated which yields an excellent initial discharge capacity of 650 mAh g^{-1} with a better cyclic stability and rate capability. To our knowledge, the self-induced active SEI layer formation is a novel finding in this article which facilitates lithium-ion diffusion across the interface, protects the electrode surface and supports for excellent electrochemical performance.

Results and Discussion

Synthesis of (Hematite)- $\alpha\text{-Fe}_2\text{O}_3$ nanosheet has been accomplished using the Pechini method, followed by post-calcination processes. Subsequently, sulfur has been elegantly coated onto the (Hematite)- $\alpha\text{-Fe}_2\text{O}_3$, using two distinct methods: a physical method with subsequent calcination at 550°C ($\alpha\text{-Fe}_2\text{O}_3@\text{S-1}$) and a physical method followed by microwave assistance ($\alpha\text{-Fe}_2\text{O}_3@\text{S-2}$) processes. Scheme S1 illustrates the synthesis of Fe_2O_3 nanosheets and the remaining two Schemes S(2–3) illustrate the sulfur coating by post-calcination and microwave assisted methods. The active materials of as-prepared bare $\alpha\text{-Fe}_2\text{O}_3$ and sulfur coated $\alpha\text{-Fe}_2\text{O}_3$ such as $\alpha\text{-Fe}_2\text{O}_3@\text{S-1}$ and $\alpha\text{-Fe}_2\text{O}_3@\text{S-2}$ are separately taken along with conducting carbon and PVDF as a binder in a 8:1:1 ratio for fabricating the negative electrodes. In a lithium-ion coin cell assembly under argon atmosphere, each of the $\alpha\text{-Fe}_2\text{O}_3$ based electrode samples as working electrode against pure lithium metal as reference as well as counter electrode have been constructed by using a typical CR2032 cell component. The electrochemical and subsequent ex-situ measurements are carried out on these coin cells containing $\alpha\text{-Fe}_2\text{O}_3$ based electrodes. The detailed information of the initial precursor materials, synthesis procedures for bare and sulfur coated $\alpha\text{-Fe}_2\text{O}_3$, $\alpha\text{-Fe}_2\text{O}_3@\text{S-1}$ and $\alpha\text{-Fe}_2\text{O}_3@\text{S-2}$ electrode fabrication procedures, followed by coin cell construction (LIB & LISB), instrument particulars for structural, morphology, surface chemistry, electrochemical and ex-situ characterizations are elaborately discussed under Experiment Section in Supporting Information for a comprehensive understanding of this research.

The crystalline structure of the bare and coated samples has been examined by the XRD technique in the range of (2θ) 10 to 80° . Figure 1(a) shows XRD pattern of bare $\alpha\text{-Fe}_2\text{O}_3$, sulfur coated $\alpha\text{-Fe}_2\text{O}_3@\text{S-1}$ and $\alpha\text{-Fe}_2\text{O}_3@\text{S-2}$ samples. The sharp and distinct diffraction peaks (2θ) observed at 24.138° , 33.153° , 35.612° , 39.277° , 40.855° , 49.480° , 54.09° , 57.59° , 62.45° ,

63.991° , 69.60° , 71.937° , and 75.431° in both the XRD patterns of bare $\alpha\text{-Fe}_2\text{O}_3$ and $\alpha\text{-Fe}_2\text{O}_3@\text{S-2}$ are corresponding to crystallographic planes (012), (104), (110), (006), (113), (024), (116), (018), (214), (300), (208), (1010), and (220) of $\alpha\text{-Fe}_2\text{O}_3$ respectively (ICDD: 00-033-0664).^[36–38] Whereas the XRD pattern of $\alpha\text{-Fe}_2\text{O}_3@\text{S-1}$ shows slightly different diffraction peaks (2θ) as observed at 35.612° , 39.277° , 40.855° , 54.09° , 57.59° and 69.60° which are corresponding to crystallographic planes of (110), (006), (113), (116), (018) and (208), respectively for $\alpha\text{-Fe}_2\text{O}_3$. The observed diffraction peaks of $\alpha\text{-Fe}_2\text{O}_3@\text{S-1}$ are in best match with ICDD: 00-033-0664, which corresponds to the development of the rhombohedral crystal structure of pristine $\alpha\text{-Fe}_2\text{O}_3$ within which the Fe^{3+} cation occupies 2/3 octahedral sites in close-packed oxygen lattice and crystallize in R3c space group.

In sulfur-coated samples ($\alpha\text{-Fe}_2\text{O}_3@\text{S-1}$ and $\alpha\text{-Fe}_2\text{O}_3@\text{S-2}$), the presence of sulfur is clearly confirmed by diffraction peaks (2θ) observed at 11.498° , 15.589° , 21.874° , 22.724° , 23.083° , 25.879° , 26.347° , 26.750° , 27.769° , 28.681° , 28.967° , 29.160° , 33.305° , 33.498° , 35.877° , 45.234° , 51.254° , 52.102° , 53.045° , 55.368° , and 55.770° , which are corresponding to crystallographic planes (111), (022), (220), (131), (222), (026), (224), (311), (040), (313), (135), (008), (331), (242), (244), (353), (266), (535), (602), (2014), and (359), respectively for sulfur (ICDD: 00-008-0247).^[39,40] It is interesting to note in both the sulfur-coated samples that there are two new prominent but less intense diffraction peaks (2θ) observed at 37.107° and 56.279° corresponding to (210) and (311) planes, respectively which might be due to the FeS_2 (ICDD No: 00-042-1340)^[41] formation at the interface of $\alpha\text{-Fe}_2\text{O}_3$ and sulfur. However, the XRD pattern for sulfur-coated samples show no other peaks attributed to FeS_2 , indicating that there might be suppressed FeS_2 phase formation.

To better examine the morphology, the synthesized powdered samples have been examined by using a High-Resolution Scanning Electron Microscope (HR-SEM) and further magnification with a High-Resolution Transmission Electron Microscope (HR-TEM). Figure (S1–S3), in supporting information, shows the HR-SEM image of as-synthesized bare $\alpha\text{-Fe}_2\text{O}_3$, sulfur-coated $\alpha\text{-Fe}_2\text{O}_3@\text{S-1}$ and $\alpha\text{-Fe}_2\text{O}_3@\text{S-2}$ samples. Figure S1(a and b) shows a gray scale image, manifesting a sheet-like morphology of bare $\alpha\text{-Fe}_2\text{O}_3$, and Figure S1(c and d) shows the elemental mapping that confirms the uniform distribution of elements such as Iron (Fe) and Oxygen (O). These results strongly suggest forming a single-phase pure $\alpha\text{-Fe}_2\text{O}_3$ without any foreign elements. Figure S2(a and b) observes the nano-sheet morphology of sulfur-coated Iron oxide ($\alpha\text{-Fe}_2\text{O}_3@\text{S-1}$), and its elemental mapping reveals the uniform sulfur coating on the surface of $\alpha\text{-Fe}_2\text{O}_3$ nanosheet. Additionally, the corresponding elemental mapping as shown in Figure S2(c–e), illustrates the organized distribution of elements such as Iron, Oxygen, and Sulfur in $\alpha\text{-Fe}_2\text{O}_3@\text{S-1}$. Figure S3(a and b) depicts the nanosheet morphology of sulfur-coated Iron oxide ($\alpha\text{-Fe}_2\text{O}_3@\text{S-2}$) featuring embedded irregular needle-like particles. The corresponding elemental mapping indicates the homogeneous distribution of elements, including Fe, O, and S in the $\alpha\text{-Fe}_2\text{O}_3@\text{S-2}$ powder samples as evidenced in Figure S3(c–e). HR-SEM images of as-synthesized bare and sulfur coated $\alpha\text{-Fe}_2\text{O}_3$ samples revealed nanosheet morphology and the elemental

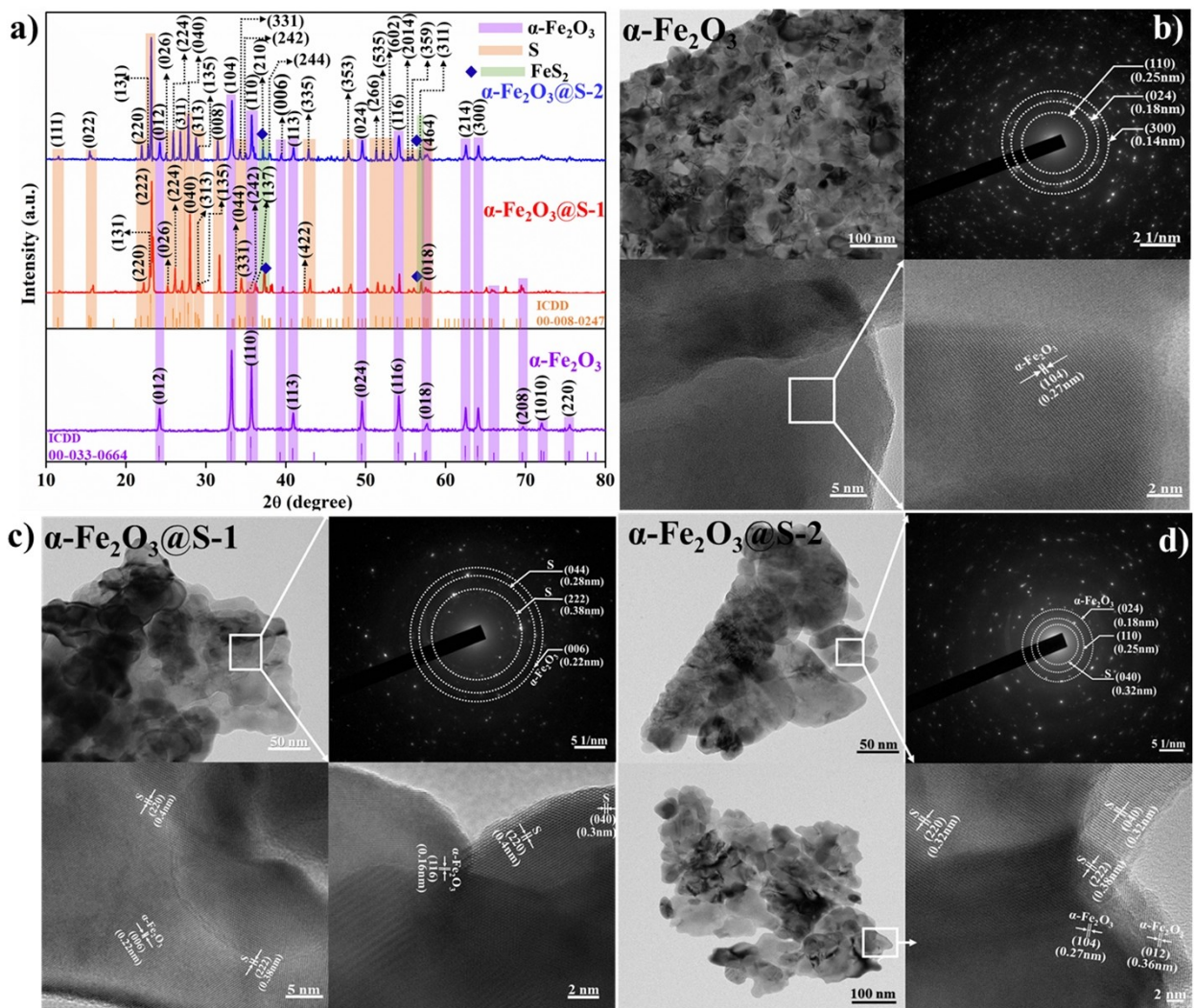


Figure 1. PXRD and HRTEM analyses of as-synthesized α -Fe₂O₃, α -Fe₂O₃@S-1, and α -Fe₂O₃@S-2. a) PXRD pattern of bare and sulfur coated α -Fe₂O₃. b, c, and d) HRTEM morphologies and SAED pattern of bare α -Fe₂O₃ and coated α -Fe₂O₃@S-1 and α -Fe₂O₃@S-2 nanosheets.

mapping confirms the presence of sulfur coating in the relevant samples.

To examine the structural evolution and detailed insights of the dimensional morphology of as-synthesized bare and sulfur coated α -Fe₂O₃ samples, an HRTEM analysis has been employed. Figure 1(b) shows HR-TEM images at different magnifications and the SAED pattern of bare α -Fe₂O₃ sample. The surface morphology depicts the formation of a bare α -Fe₂O₃ nanosheet with an average particle size of ~140 nm. The SAED pattern corresponding to the circled region reveals the existence of (110), (204), and (300) crystallographic planes corresponding to the pure α -Fe₂O₃ phase with an interplanar distance $d=0.25$,^[42,43] 0.18, and 0.14 nm, respectively. The marked lattice fringes region corresponding to the (104) plane with an interplanar spacing of $d=0.27$ nm further substantiates the pure phase of α -Fe₂O₃.^[44] Figure 1(c) shows the nanosheet morphology of as-synthesized α -Fe₂O₃@S-1, which exhibits an average particle size of ~61 nm with sulfur coating thickness of ~9 nm. The SAED pattern of α -Fe₂O₃@S-1 reveals dark spots,

indicating the formation of two distinct polycrystalline structures attributed to the (044) and (222) planes of sulfur with an interplanar distance $d=0.28$ and 0.38 nm^[45] whereas the (006) plane is corresponding to α -Fe₂O₃ nanosheet with an interplanar distance of $d=0.22$ nm.^[46] The inner set of dark spots results in the sulfur formation, while the outer set of encircled dark spots, represents the α -Fe₂O₃ formation. Observing the high-resolution lattice fringes (i.e., at 2 and 5 nm scale), the interplanar distances of $d=0.4$, 0.3 and 0.38 nm are corresponding to the (220), (040) and (222) planes of sulfur respectively, while the interplanar distances of $d=0.22$, and 0.16 nm are attributed to the (006), and (116) plane of α -Fe₂O₃, respectively.^[46] Figure 1(d) shows a gray image resulting in the nanosheet formation of α -Fe₂O₃@S-2 with an average particle size of about ~65 nm with asulfur coating thickness of around ~8 nm. The SAED pattern of α -Fe₂O₃@S-2 reveals the two distinct polycrystalline structures corresponding to the (024) and (110) planes, featuring interplanar spacing $d=0.18$ and 0.25 nm, respectively, attributed to the α -Fe₂O₃ nanosheet formation. The

inner dark spot is corresponding to the (040) plane with an interplanar distance $d=0.32$ nm, indicating the sulfur formation. Furthermore, the high-resolution lattice fringes with interplanar distances of $d=0.32$, 0.38, and 0.32 nm are corresponding to the (220), (222),^[45] and (040) planes of sulfur, respectively, and interplanar distances of $d=0.27$ and 0.36 nm are indexed to the (104)^[47] and (012) planes of $\alpha\text{-Fe}_2\text{O}_3$, respectively. The crystalline phases and their corresponding d-spacing results obtained from HR-TEM analysis are in con-

currence with the XRD results, affirming the presence of phase pure bare and sulfur-coated $\alpha\text{-Fe}_2\text{O}_3@S-1$ and S-2.

The presence of oxygen defects (ODs) in both the as-synthesized bare and coated $\alpha\text{-Fe}_2\text{O}_3$ samples have been further investigated by using HR-TEM. The presence of oxygen defects might be attributed to the potential release of carbon dioxide (CO_2) during the chemical reaction occurred when citric acid and ethylene glycol are introduced in the synthesis processes of Hematite- $\alpha\text{-Fe}_2\text{O}_3$ nanosheet. Figure 2(a) shows HR-TEM of bare $\alpha\text{-Fe}_2\text{O}_3$ revealing their morphology characterized by small pits

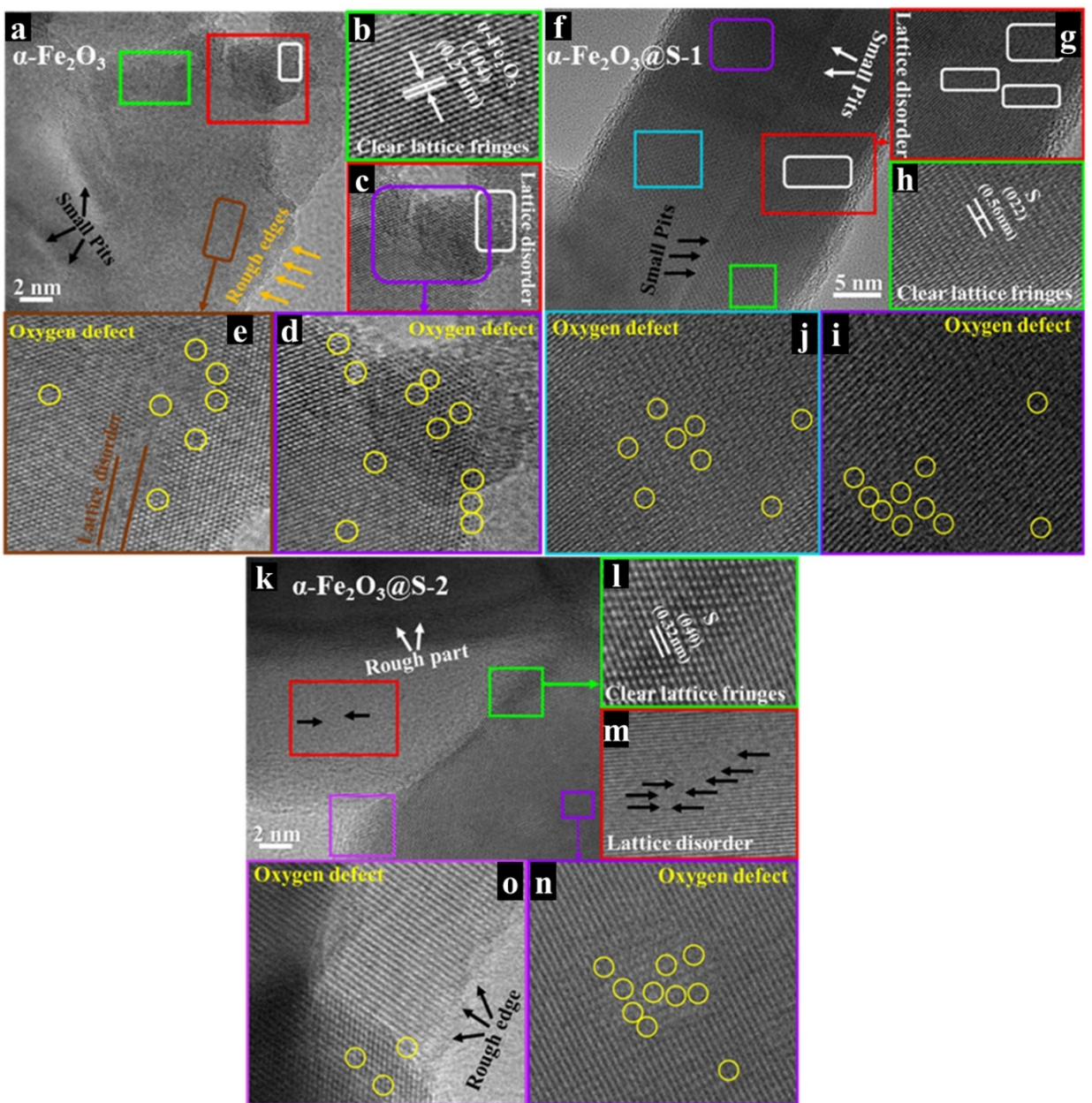


Figure 2. HRTEM analysis of Oxygen defects in as-synthesized powdered samples of $\alpha\text{-Fe}_2\text{O}_3$, $\alpha\text{-Fe}_2\text{O}_3@S-1$, and $\alpha\text{-Fe}_2\text{O}_3@S-2$. a) HR-TEM morphology for small pits and rough edges in bare $\alpha\text{-Fe}_2\text{O}_3$ nanosheet, b) clear lattice fringes in bare $\alpha\text{-Fe}_2\text{O}_3$ nanosheet, c) Lattice disorder in $\alpha\text{-Fe}_2\text{O}_3$ nanosheet morphology, d) enlarged HR-TEM image highlighting oxygen defect in bare $\alpha\text{-Fe}_2\text{O}_3$ nanosheet, e) enlarged image of oxygen defect and lattice disorder in the bare $\alpha\text{-Fe}_2\text{O}_3$; f) small pits in $\alpha\text{-Fe}_2\text{O}_3@S-1$ nanosheet, g) lattice disorder in $\alpha\text{-Fe}_2\text{O}_3@S-1$ nanosheet morphology, h) clear lattice fringes in the $\alpha\text{-Fe}_2\text{O}_3@S-1$ nanosheet, i,j) highlights oxygen defect sites in $\alpha\text{-Fe}_2\text{O}_3@S-1$; k) rough portion of $\alpha\text{-Fe}_2\text{O}_3@S-2$, l-m) clear lattice fringes and lattice disorder in $\alpha\text{-Fe}_2\text{O}_3@S-2$, n-o) oxygen defects in $\alpha\text{-Fe}_2\text{O}_3@S-2$ nano sheet.

and nearby rough edges indicated by black and orange arrows. These features also significantly contribute to the oxygen defects formed in the as-synthesized bare $\alpha\text{-Fe}_2\text{O}_3$ sample. Figure 2(b) of bare $\alpha\text{-Fe}_2\text{O}_3$ sample indicates the perfect lattice arrangement of as-synthesized bare Hematite- $\alpha\text{-Fe}_2\text{O}_3$ nanosheet, with a d -spacing of $d=0.27\text{ nm}$ corresponding to the (104) plane of bare $\alpha\text{-Fe}_2\text{O}_3$.^[47] Figure 2(c) shows the enlarged HR-TEM images of the as-synthesized bare $\alpha\text{-Fe}_2\text{O}_3$ nanosheet indicates the lattice disorder and oxygen defects sites within the $\alpha\text{-Fe}_2\text{O}_3$ nanosheet. The lattice disorder arises from the rough surface and small pit scale which are indicated by white and purple boxes. The enlarged HR-TEM images (Figure 2d,e), revealing the oxygen defects at various portions on the bare $\alpha\text{-Fe}_2\text{O}_3$ nanosheet. The observed lattice disorder and dislocation indicate the oxygen vacancies in the as-synthesized samples. Oxygen defects are pivotal in enhancing electronic and ionic conductivity so that to improve lithium-ion kinetics. They lead to an uneven charge distribution surrounding the vacancy, resulting in an additional coulombic force that facilitates the migration of lithium ions. Figure 2(f-j) presents HRTEM images which depicts the nanosheet morphology of sulfur-coated iron oxide ($\alpha\text{-Fe}_2\text{O}_3@\text{S-1}$). Within these HR-TEM images, small pits in various regions are discernible and indicated by black and white arrows. Those small pits could potentially contribute to the formation of oxygen vacancies in the as-synthesized $\alpha\text{-Fe}_2\text{O}_3@\text{S-1}$ sample. Figure 2(g) depicts the enlarged image of the as-synthesized $\alpha\text{-Fe}_2\text{O}_3@\text{S-1}$ nanosheet highlighted within a white box. This HR-TEM image reveals mild lattice disorder, and dislocations as observed at different portions in as-synthesized $\alpha\text{-Fe}_2\text{O}_3@\text{S-1}$ nanosheet. The main reason for this lattice disorder may be attributed to the rough or uneven surface of the nanosheet. Figure 2(h) indicates the perfect lattice arrangement of sulfur-coated $\alpha\text{-Fe}_2\text{O}_3$ nanosheet, with a d spacing of 0.56 nm corresponding to the (022) plane of sulfur. Figure 2(i,j) shows magnified HR-TEM images of $\alpha\text{-Fe}_2\text{O}_3@\text{S-1}$ nanosheet which reveal lattice disorder and dislocations, notably highlighted within yellow-circled regions, indicates the presence of oxygen vacancies. The HR-TEM image (Figure 2k) of $\alpha\text{-Fe}_2\text{O}_3@\text{S-2}$ sample exhibits a rough surface with lattice disorder, and overlap of nanosheets which contribute to the formation of oxygen defects as highlighted by white and black arrows. Figure 2(l) depicts the enlarged image of nanosheet corresponding to the green box which reveals perfect lattice arrangement of the as-synthesized $\alpha\text{-Fe}_2\text{O}_3@\text{S-2}$ nanosheet. Specifically, the lattice spacing measured as $d=0.32\text{ nm}$ in Figure 2(l) corresponds to the (040) plane of sulfur. Figure 2(m) shows a enlarged HR-TEM image which depicts lattice fringes in the as-synthesized $\alpha\text{-Fe}_2\text{O}_3@\text{S-2}$ nanosheet, revealing lattice disorder as indicated by black arrows. This observed disorder in the $\alpha\text{-Fe}_2\text{O}_3@\text{S-2}$ lattice may be attributed to the rough surface and overlapping nanosheets. Furthermore, the purple boxes in the enlarged HR-TEM image (Figure 2k) reveal the presence of rough edges (denoted by black arrows) and oxygen defects at various locations as indicated by yellow circles in Figure 2 (n and o), which are clear evidence of oxygen vacancies in the as-synthesized $\alpha\text{-Fe}_2\text{O}_3@\text{S-2}$ nanosheet. As observed from the HR-TEM images, the presence of oxygen defects in iron oxide could

possibly enhance the electronic conductivity and electrochemical performance in both the bare and sulfur-coated samples.

The surface chemistry of as-synthesized bare $\alpha\text{-Fe}_2\text{O}_3$ and sulfur coated $\alpha\text{-Fe}_2\text{O}_3@\text{S-1}$ and $\alpha\text{-Fe}_2\text{O}_3@\text{S-2}$ samples has been evaluated by using XPS analysis to confirm the oxidation state of the elements. The survey spectra of as-synthesized bare $\alpha\text{-Fe}_2\text{O}_3$ and sulfur coated $\alpha\text{-Fe}_2\text{O}_3@\text{S-1}$ and $\alpha\text{-Fe}_2\text{O}_3@\text{S-2}$ are given in Figure S4(a and b) which implies related to the corresponding samples the presence of Fe, O, and S elements related to the respective samples in the binding energy (BE) range of about 0–1200 eV. Figure 3(a–c) shows the core level Fe 2p XPS spectra of bare, sulfur coated $\alpha\text{-Fe}_2\text{O}_3@\text{S-1}$ and $\alpha\text{-Fe}_2\text{O}_3@\text{S-2}$ samples in the BE range of 705 to 740 eV. The Fe 2p spectra depicts two strong peaks in the binding energy range of 710.7 and 724.1 eV with an energy separation of 13.4 eV for all the samples, which is corresponding to the Fe 2p_{3/2} and Fe 2p_{1/2} signals from $\alpha\text{-Fe}_2\text{O}_3$.^[48] The signals of Fe are deconvoluted into a triplet of each signals Fe 2p_{3/2} and Fe 2p_{1/2} which represent a mixed valence state of Fe³⁺ and Fe²⁺ of Iron. These two oxidation states of Fe³⁺ and Fe²⁺ of Fe 2p_{3/2} appears at 710.3 eV and 709.3, 712.3 eV for all the samples ($\alpha\text{-Fe}_2\text{O}_3$, $\alpha\text{-Fe}_2\text{O}_3@\text{S-1}$ and $\alpha\text{-Fe}_2\text{O}_3@\text{S-2}$). In Fe 2p_{1/2} the mixed oxidation states of Fe³⁺ and Fe²⁺ are appeared at ~724.9 eV for bare and $\alpha\text{-Fe}_2\text{O}_3@\text{S-1}$ samples while that of 725.5 eV^[49] for $\alpha\text{-Fe}_2\text{O}_3@\text{S-2}$. In all the bare and sulfur coated $\alpha\text{-Fe}_2\text{O}_3$ samples, the significant peak observed at 710.3 eV is assigned to the octahedrally coordinated Fe³⁺ ions of the hematite phase of $\alpha\text{-Fe}_2\text{O}_3$. The peak centred at ~709.4 eV of all the samples is attributed to Fe²⁺ ions which engage octahedral sites, and also peak located at ~712 eV for all the samples are attributed to tetrahedrally coordinated Fe³⁺ ions of the magnetite phase. The appearance of peaks at ~709.4 and ~712.3 eV for all the samples might be due to the existence of a magnetite phase and the maghemite kind of structure. The structure retained at the surface of the particles and survived through the heat treatment as similarly reported by Bora et al.^[50] In Fe 2p spectra, the appearance of two satellite peaks in the energy range of ~719 and ~733 eV for all the samples are corresponding to Fe 2p_{3/2} and Fe 2p_{1/2} which reveals the presence of dominant Fe³⁺ in $\alpha\text{-Fe}_2\text{O}_3$.^[51] The core level O 1s XPS spectra of bare and sulfur coated samples as shown in Figure 3(d–f), indicates a peak centered at ~529.8 eV for all the samples which is attributed to the BE of Fe–O bond.^[52,53] The oxygen defects are indicated by the oxygen vacancies peak centered in the energy range of ~531.3 eV.^[51,52,54,55] The presence of oxygen defect peak in all the samples might be due to the slight lattice disorder followed by dislocations of $\alpha\text{-Fe}_2\text{O}_3$ as evidenced in HR-TEM analysis.

Figure 3g shows XPS high resolution spectrum of $\alpha\text{-Fe}_2\text{O}_3@\text{S-1}$ which indicates a S 2p peak centred at 163.8 eV with a shoulder peak. The S 2p peak appeared for $\alpha\text{-Fe}_2\text{O}_3@\text{S-1}$ sample is deconvoluted into two peaks corresponding to S 2p_{1/2} and S 2p_{3/2} at the binding energy of 163.8 eV^[56–58] and 162.7 eV, respectively. The most intense peak of $\alpha\text{-Fe}_2\text{O}_3@\text{S-1}$ sample is centred at the binding energy of 163.8 eV (S 2p_{1/2}) which is assigned to the S–S bond corresponding to the sulfur dimer present in the FeS₂ inter-particle layer component. The shoulder peak centred at 162.7 eV is assigned to S 2p_{3/2} which might be

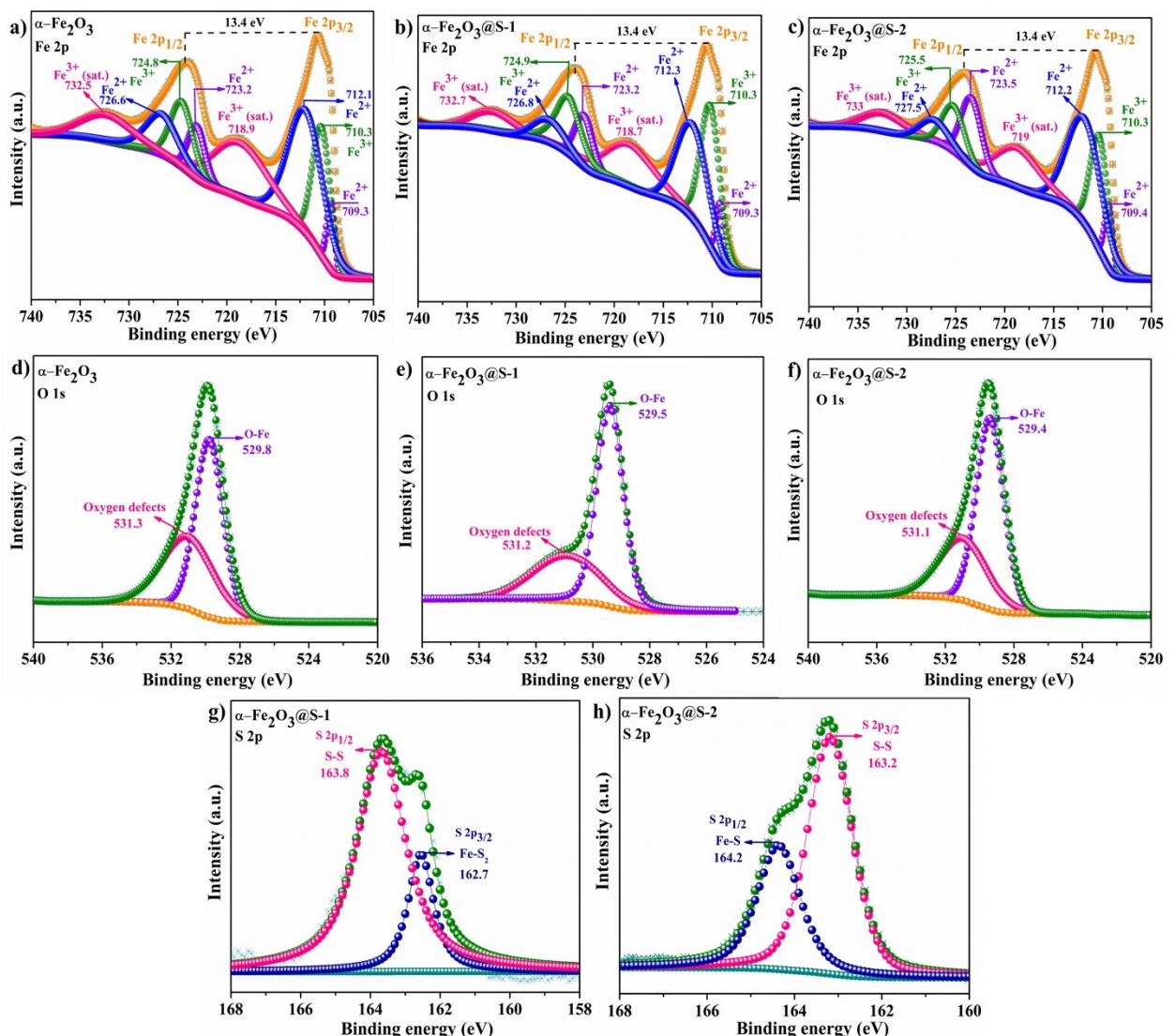


Figure 3. X-ray Photoelectron Spectra of as-synthesized bare $\alpha\text{-Fe}_2\text{O}_3$ and Sulfur coated $\alpha\text{-Fe}_2\text{O}_3@\text{S-1}$ and $\alpha\text{-Fe}_2\text{O}_3@\text{S-2}$ samples in the energy range of (a-c) $\alpha\text{-Fe}_2\text{O}_3$ 2p, (d-f) O 1s and (g-h) S 2p signals.

due to the disulfide group of iron pyrite (i.e., FeS_2)^[59–61] at the inner spherical surface of sulfur bound to 'Fe' on the top surface of Fe_2O_3 particle. In the case of $\alpha\text{-Fe}_2\text{O}_3@\text{S-2}$ sample, high resolution XPS spectrum (Figure 3h) shows the appearance of high intense S 2p peak centred at 163.2 eV along with a satellite peak. The S 2p broad peak is deconvoluted into two peaks at the binding energy of 164.2 eV and 163.2 eV which are corresponding to a doublet representing spin-orbital of S 2p_{1/2} and S 2p_{3/2}, respectively. The peak observed at the higher binding energy of 164.2 eV (S 2p_{1/2}) is attributed to the bonding of Fe–S (inter particle layer- FeS_x).^[62–65] The second peak located at the binding energy of 163.2 eV (S 2p_{3/2}) is assigned to the S–S bond at the surface of sulfur particulates.^[66,67] In the S1 sample, the appearance of S–S sulfur dimer is corresponding to the S–S bond present in FeS_2 component which could be the reason for appearance of S–S bond in the higher binding energy range. The S–S bond in S2 sample indicates the sulfur bond present at the surface of sulfur which might be the reason

for the appearance of S–S bond in the lower binding energy range compared to S1 sample.

Figure 4(a-f) shows the cyclic voltammogram (CV) results exhibiting the kinetics of Li^+ insertion/de-insertion in both bare and sulfur-coated $\alpha\text{-Fe}_2\text{O}_3$ electrode materials with in a potential range of 0.0 to 3.0 V at 0.1 mVs⁻¹ vs Li^+/Li . Figure 4(a and b) exhibits CV curves of bare $\alpha\text{-Fe}_2\text{O}_3$ nanosheet vs Li^+/Li for the first five cycles. During the first negative scan, a slight cathodic hump is observed at 1.7 V, which might be attributed to the initial lithium-ion intercalation from pure lithium metal to bare $\alpha\text{-Fe}_2\text{O}_3$ due to the Fe^{3+} to Fe^{2+} reduction that leads to the formation of $\text{Li}_2\text{Fe}_2\text{O}_3$ as indicated in equation (1). A broad and deep cathodic peak emerges at 0.67 V^[68] might be attributed to the Li^+ ion intercalation into $\alpha\text{-Fe}_2\text{O}_3$ due to further multi-step reduction of Fe^{2+} to Fe^0 contributing formation of metallic Fe along with reversible amorphous Li_2O by conversion reaction mechanism. Furthermore, this deep shallow broad peak is also associated with irreversible Li^+ capture by surface-adsorbed air

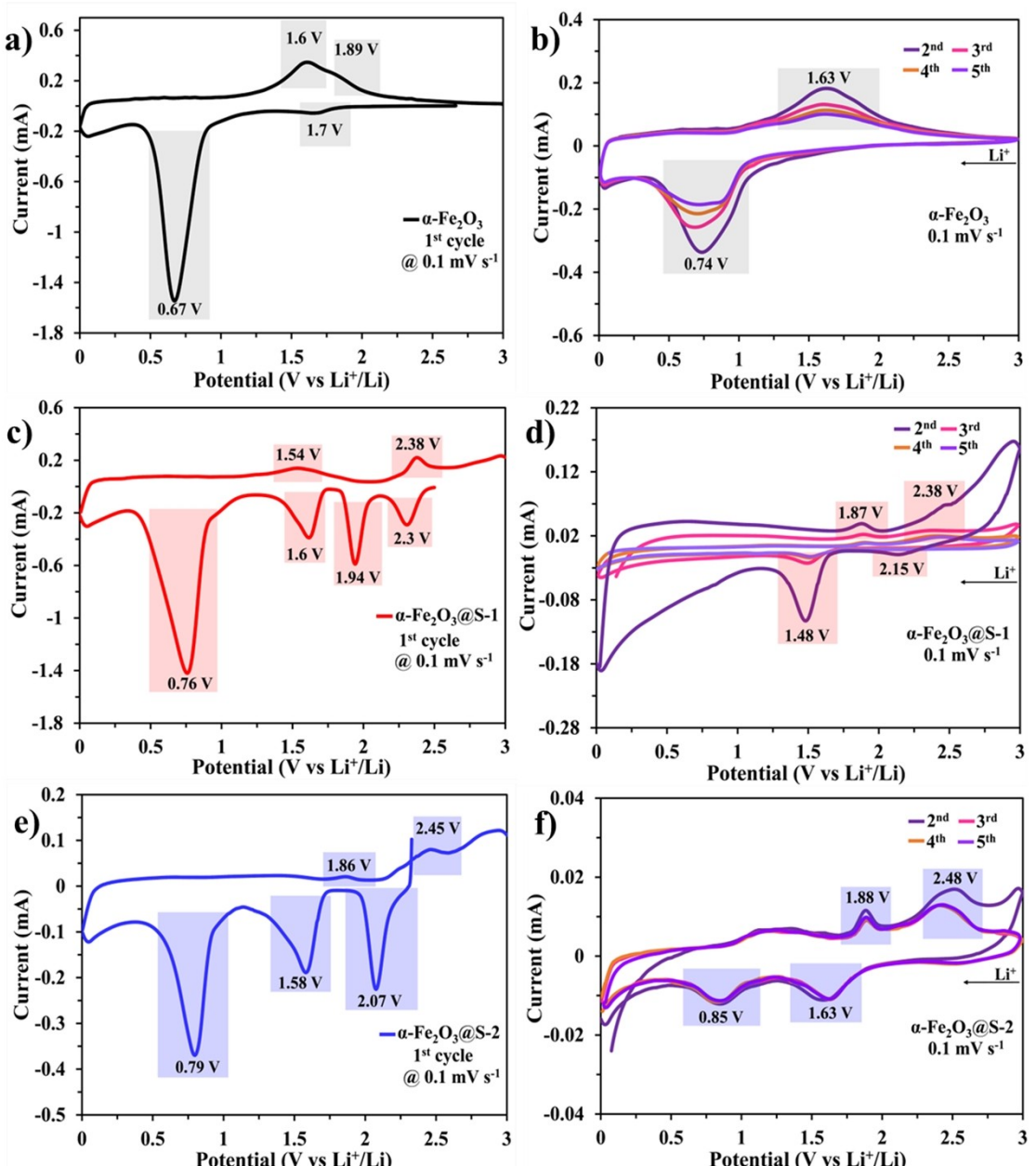


Figure 4. CV curves of a) initial cycle of bare $\alpha\text{-Fe}_2\text{O}_3$, and b) 2nd to 5th cycle of bare $\alpha\text{-Fe}_2\text{O}_3$ vs Li^+/Li at 0.1 mVs^{-1} . c) initial cycle of $\alpha\text{-Fe}_2\text{O}_3@\text{S-1}$, and d) 2nd to 5th cycles of sulfur coated $\alpha\text{-Fe}_2\text{O}_3@\text{S-1}$ vs Li^+/Li at 0.1 mVs^{-1} . e) initial cycle of $\alpha\text{-Fe}_2\text{O}_3@\text{S-2}$ and f) 2nd to 5th cycles of $\alpha\text{-Fe}_2\text{O}_3@\text{S-2}$ versus Li^+/Li at 0.1 mVs^{-1} .

molecules, leading to the undesired SEI formation on the surface of the $\alpha\text{-Fe}_2\text{O}_3$ working electrode. In the reverse scan, a significant sharp anodic peak is observed at 1.6 V along with a small hump at 1.89 V, which are correlated with the two step oxidation processes of Fe^0 to Fe^{2+} and Fe^{2+} to Fe^{3+} [11], respectively. During the first step of oxidation (i.e., Fe^0 to Fe^{2+}), the metallic 'Fe' reacts with Li_2O to form $\text{Li}_2\text{Fe}_2\text{O}_3$ in which 4Li^+ ions are released as shown in equation (2). In the further oxidation process, most of the Fe^{2+} in $\text{Li}_2\text{Fe}_2\text{O}_3$ are oxidized into Fe^{3+} at 1.89 V which de-intercalates $x\text{Li}^+$ ions and simultaneously gets converted into an alloy of $\text{Li}_{(2-x)}\text{Fe}_{(2-x)}\text{Fe}_x\text{O}_3$ as demonstrated in equation (3).

Based on the redox pattern, a part of lithium-ion might be retained with Fe_2O_3 structure in the form of an alloy as explained above. In the second cycle, only a prominent broad but with less intense cathodic peak corresponding to multi-step Fe^{3+} reduction to Fe^0 is observed at 0.74 V which is then shifted to 0.69 V upon further cycling. A sudden decrease in intensity of shallow cathodic peak implies alleviation of SEI formation due to relative stabilization. Though the cathodic peaks are aligned at 0.69 V from 3rd to 5th cycle without further shifts, the intensity of the peak is gradually decreasing which indicates inability of intercalating/accommodating sufficient lithium-ion for the conversion reaction mechanism as the portion of lithiated iron oxide alloy retains from the previous cycle. The

anodic scans of 2nd to 5th cycles indicate a broad oxidation peak centred at 1.63 V with a slight hump at 1.8 V which reveals the multi-step oxidation process as described above. The slight deviation in redox peaks in the initial cycles reveals electrochemical alterations and structural reconstruction in the $\alpha\text{-Fe}_2\text{O}_3$ working electrode in response to the Li^+/Li redox reactions. Remarkably, from the 3rd to 5th cycles, the redox peaks are consistently aligned in the $\alpha\text{-Fe}_2\text{O}_3$ working electrode which reveals, strong redox performance and stable cycling characteristics.^[29] However, the decrease in the intensity of the redox peaks upon further cycles indicate additional lithium-ion trapping in the $\text{Li}_{(2-x)}\text{Fe}_{(2-x)}\text{Fe}_x\text{O}_3$ ($x < 2$) structure so that the amount of $x\text{Li}^+$ de-intercalation decreases. The following equations indicate the possible redox kinetics of lithium-ion in Fe_2O_3 :

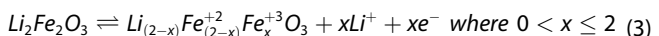
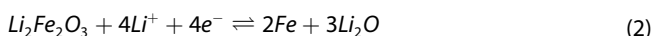
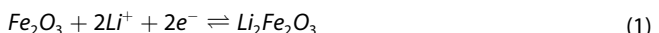
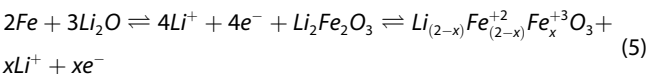
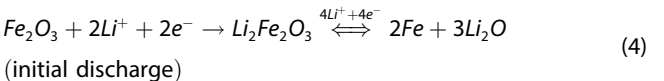
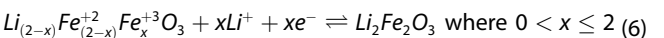


Figure 4(c and d) shows the cyclic voltammogram profile of the $\alpha\text{-Fe}_2\text{O}_3@\text{S-1}$ electrode during the first five cycles. The initial discharge sweep indicates sharp cathodic peaks at 2.3, 1.94, and 1.6 V which are attributed to the lithium intercalation into the $\alpha\text{-Fe}_2\text{O}_3@\text{S-1}$ working electrode. The $\alpha\text{-Fe}_2\text{O}_3@\text{S-1}$ exhibits two new cathodic peaks at higher potential regions during the initial lithium intercalation processes compared to bare $\alpha\text{-Fe}_2\text{O}_3$. These new peaks correspond to the interaction of lithium ions with the surface-coated sulfur in the $\alpha\text{-Fe}_2\text{O}_3@\text{S-1}$ electrode, possibly forming an active Li_xSO_y based SEI species in the $\alpha\text{-Fe}_2\text{O}_3@\text{S-1}$ electrode. Interestingly, the intensity of the reduction peak observed at 1.6 V corresponding to $\text{Li}_2\text{Fe}_2\text{O}_3$ alloy formation resulted from $\text{Fe}^{3+} \rightarrow \text{Fe}^{2+}$ reduction is higher than the bare $\alpha\text{-Fe}_2\text{O}_3$ electrode which indicates a well-defined intercalation process in the $\alpha\text{-Fe}_2\text{O}_3@\text{S-1}$ electrode. This process supports intercalation of 2Li^+ into the Fe_2O_3 structure as shown in equation (4). In addition to the above peaks, a prominent shallow reduction peak appeared at 0.76 V similar to bare $\alpha\text{-Fe}_2\text{O}_3$ which might be attributed to further reduction of Fe^{2+} to Fe^0 resulting the formation of metallic 'Fe' accompanied with Li_2O through conversion reaction. This process facilitates further lithium-ion intercalation that enables the occurrence of conversion reaction as demonstrated in equation (4). The nature of deep shallow reduction peak observed at 0.76 V also indicates the reduction of much Li^+ ion with surface adsorbed air molecules that leads to the formation of inter-metallic irreversible SEI layer on the surface of the electrode as discussed above. The anodic scan shows significant firm oxidation peaks at 1.54 and 2.38 V corresponds to the oxidation of Fe^0 to Fe^{2+} and Fe^{2+} to Fe^{3+} , respectively which reveals the conversion reaction of Fe with Li_2O for the formation of $\text{Li}_2\text{Fe}_2\text{O}_3$ followed by $\text{Li}_{(2-x)}\text{Fe}_{(2-x)}\text{Fe}_x\text{O}_3$ associated with multi-step de-intercalation of $(4+x)\text{Li}^+$ ($x < 2$) from sulfur coated $\alpha\text{-Fe}_2\text{O}_3$ as demonstrated in equation (5). The overall redox reaction may be written in combination of equation (1–3) as follows;



where $0 < x \leq 2$. These redox reactions are in good agreement and analogy with the earlier literature reports.^[69,70]

Figure 4(d) shows CV plots of $\alpha\text{-Fe}_2\text{O}_3@\text{S-1}$ working electrode for 2nd to 5th cycle. In the second cycle, the two initial cathodic peaks observed at 2.3 and 1.94 V are replaced by a minor cathodic peak at ~2.15 V which might be due to a quasi-reversible Li–S based component within the working electrode. In addition, this reduction peak at 2.15 V might also indicate that there might be further concurrent Li_xSO_y active SEI formation that surprisingly nullifies further formation of undesirable SEI as evidenced from the disappearance of shallow reduction peak at 0.76 V. The reduction peak observed at 1.6 V in the initial scan gets shifted to 1.48 V as a well-defined prominent peak which might be due to the reduction of Fe^{3+} to Fe^{2+} leading to the intercalation of $x\text{Li}^+$ into the $\text{Li}_{(2-x)}\text{Fe}_{(2-x)}\text{Fe}_x\text{O}_3$. Only a sloppy region with a small hump at 0.85 V is observed in the lower potential which might be due to the Fe^{2+} to Fe^0 reduction corresponds to the conversion reaction, however this region completely disappeared upon further cycles due to the favourable electrochemical alteration in the structure for redox reactions. Subsequently, two significant anodic peaks emerge at 1.87 and 2.38 V in the anodic scan in which the first oxidation peak is reflecting the combined two-step oxidation processes (Fe^0 to Fe^{2+} and Fe^{2+} to Fe^{3+}) leading to the de-intercalation of $(4+x)\text{Li}^+$ as that of equation (5). The second oxidation peak observed at higher potential might be due to the quasi reversible component of Li–S as discussed earlier which gets disappeared upon further scans. In the subsequent cycles, only a consistently aligned pair of cathodic and anodic peak is observed at 1.49 and 1.88 V, respectively whereas it's noteworthy that the lower potential reduction peak corresponding to conversion reaction is completely disappeared. This peculiar behaviour of the electrode clearly indicates that the redox kinetics of Li^+ ion in progressive cycles are only possible with the $\text{Li}_{(2-x)}\text{Fe}_{(2-x)}\text{Fe}_x\text{O}_3$ alloy as demonstrated in equation (6) while the further conversion reaction is suppressed.



Significantly, from the 3rd to 5th cycles, the consistent alignment of redox peaks in the $\alpha\text{-Fe}_2\text{O}_3@\text{S-1}$ electrode, demonstrating robust redox properties and cyclic stability in this electrode material.

Figure 4(e and f) depicts the CV results of $\alpha\text{-Fe}_2\text{O}_3@\text{S-2}$ working electrode covering the potential window of 0.0 to 3.0 V at a sweep rate of 0.1 mV s^{-1} . The negative scan shows substantial reduction peaks at 2.07, 1.58 and 0.79 V. The higher

potential reduction peak observed at 2.07 V indicates the formation of Li_xSO_y SEI layer during the initial cycle, which disappeared in the further progressive cycles. The later reduction peak at 1.58 V might be due to the initial Li^+ intercalation into the $\alpha\text{-Fe}_2\text{O}_3@\text{S-2}$ working electrode leading the formation of $\text{Li}_2\text{Fe}_2\text{O}_3$ as discussed above. The intense reduction peak observed at 0.79 V might be due to the Fe^{2+} to Fe^0 reduction attributed to the conversion reaction as well as passive SEI layer formation by the reduction of Li^+ with the air molecules as discussed above. However, the SEI reduction peak intensity is much reduced while compared with the bare $\alpha\text{-Fe}_2\text{O}_3$ and $\alpha\text{-Fe}_2\text{O}_3@\text{S-1}$ electrodes which might be due to the effectiveness of the active Li_xSO_y layer that consumes much of the surface adsorbed oxygen and reduces the possibility passive SEI layer formation at the lower potential. The anodic scan shows two oxidation peaks at 1.86 and 2.45 V in which the first peak at 1.86 V might be attributed to the multi-step oxidation state transformation from Fe^0 to Fe^{2+} and Fe^{2+} to Fe^{3+} corresponding to the Li^+ de-intercalation process in the $\alpha\text{-Fe}_2\text{O}_3@\text{S-2}$ electrode as demonstrated in equation (5). The oxidation peak observed at 2.45 V may be due to Fe–S based reversible component which would have been synthesised during the microwave treatment. There may be Fe–S polar covalent bonding at the top layer of ‘ $\alpha\text{-Fe}_2\text{O}_3$ ’ nanosheet on which the sulfur coating is expected as a core-shell structure. The XRD analysis of $\alpha\text{-Fe}_2\text{O}_3@\text{S-2}$ sample indicates a suppressed phase of FeS_2 formation which supports the existence of Fe–S reversible component.

As shown in Figure 4(f), from second cycle onwards, the cathodic peaks are consistently shifted and aligned at 1.63 and 0.85 V while the anodic peaks are aligned at 1.88 and 2.48 V. The prominent broad cathodic peaks observed at 1.63 and 0.85 V, indicating the two-step reduction of Fe^{3+} to Fe^{2+} and Fe^{2+} to Fe^0 as demonstrated in equation (5). It should be noted that the reduction peak at 1.63 V may also be attributed to the conversion reaction of Fe–S based reversible component corresponding to the oxidation peak at 2.48 V. Indeed, it is worth noting that the shallow cathodic peak at 0.79 V gets shifted to 0.85 V in the second cycle and the intensity is abruptly diminished which indicates a stable SEI formation during the first cycle that alleviates further pile-up of SEI. There could be possibility of Li_xSO_y based active SEI layer formation, which could mitigate the formation of the undesirable SEI layer on the surface of $\text{Fe}_2\text{O}_3@\text{S-2}$ electrode. The surface-coated Li_xSO_y based SEI layer might act as a protective layer on the surface of the active material and alleviating electrolyte decomposition by circumventing the probability of direct contact of electrolyte with the active electrode. In the anodic scan, a significant oxidation peak appeared at 1.88 V might be due to the two-step oxidation process of Fe^0 to Fe^{2+} and Fe^{2+} to Fe^{3+} corresponding to the de-intercalation of Li^+ ions as demonstrated in the equation (5). The additional oxidation peak observed at 2.48 V is slightly shifted and consistently aligned at 2.4 V from 3rd cycle onwards which may be attributed to Fe–S based reversible component as compared with the earlier literatures.^[71,72] The XRD results confirm the presence of suppressed phase of FeS_x which may be formed at the interface of

Fe_2O_3 and sulfur contact region that supports for the reversible oxidation peak. Subsequently, the redox peaks exhibit consistent alignment in the following cycles without abrupt shifts, starting from the 3rd cycle onwards. This consistency highlights the excellent redox reversibility and structural integrity of the $\alpha\text{-Fe}_2\text{O}_3@\text{S-2}$ electrode. The sulfur coating on $\alpha\text{-Fe}_2\text{O}_3$ electrode by microwave method leads to enhanced electrochemical performance as evidenced in CV results. This improvement is attributed to the protective SEI layer formation ability which prevents direct contact between the electrode and the electrolyte, thereby reducing the rate of electrode deterioration.

Compared to the bare $\alpha\text{-Fe}_2\text{O}_3$ and sulfur-coated $\alpha\text{-Fe}_2\text{O}_3@\text{S-1}$ electrode, the cathodic peak observed at 0.79 V of the $\alpha\text{-Fe}_2\text{O}_3@\text{S-2}$ electrode is significantly suppressed which indicates the considerable alleviation of passive SEI layer leading to the irreversible capacity. The sulfur coating on the surface of $\alpha\text{-Fe}_2\text{O}_3@\text{S-2}$ is a protective barrier that hinders direct contact between the active $\alpha\text{-Fe}_2\text{O}_3$ material and electrolyte. This protective barrier may reduce electrolyte decomposition and act as an ion transport medium, thereby promoting the formation of a smoother, and more active Li_xSO_y based SEI layer on the surface of the $\alpha\text{-Fe}_2\text{O}_3@\text{S-2}$ electrode. The lithium-ion storage properties of bare and sulfur coated $\alpha\text{-Fe}_2\text{O}_3@\text{S-1}$ and $\alpha\text{-Fe}_2\text{O}_3@\text{S-2}$ electrodes are assessed using the GCD method in a coin-type-half cell. Figure 5(a and b) shows the charge-discharge profile of bare $\alpha\text{-Fe}_2\text{O}_3$ nanosheet over 20 and 50 cycles, at a current rate of 0.1 C and 1 C, respectively within a potential range from 0.0 to 3.0 V vs Li^+/Li . Initially, the bare $\alpha\text{-Fe}_2\text{O}_3$ electrode exhibits a discharge capacity of 946 mAh g^{-1} at a 0.1 C-rate, featuring discharge plateaus at 1.62, 0.8, 0.6, and 0.2 V. These voltage plateaus are corresponding to the initial lithium intercalation into the $\alpha\text{-Fe}_2\text{O}_3$ electrode, followed by the reduction of Fe^{3+} to Fe^0 . This phenomenon signifies the introduction of Li^+ intercalation within $\alpha\text{-Fe}_2\text{O}_3$, accompanied by the generation of reversible Li_2O by conversion reaction and SEI layer due to the reduction of Li^+ by surface adsorbed air molecules. This process leads to the forming of a SEI layer on the surface of the bare $\alpha\text{-Fe}_2\text{O}_3$ electrode, as evidenced by the CV curve of the bare $\alpha\text{-Fe}_2\text{O}_3$ electrode.

The initial discharge capacity of the bare $\alpha\text{-Fe}_2\text{O}_3$ electrode is found to be 701 mAh g^{-1} at 1 C rate, with the discharge plateau at 1.61 and 0.67 V, as shown in Figure 5(b). These cathodic plateaus are corresponding to the rapid reduction of Fe^{3+} to Fe^0 that is driven by fast lithium-ion kinetics at the 1 C rate. During the second discharge cycle, the bare $\alpha\text{-Fe}_2\text{O}_3$ electrode delivers a specific discharge capacity of 467 mAh g^{-1} at 0.1 C and of 309 mAh g^{-1} at 1 C-rate. Charge-specific capacity at the initial cycle of the bare $\alpha\text{-Fe}_2\text{O}_3$ electrode is 467 mAh g^{-1} for 0.1 C and 315 mAh g^{-1} at 1 C rate. The substantial initial discharge capacity fading (ICF) observed for bare $\alpha\text{-Fe}_2\text{O}_3$ electrodes at both 0.1 C and 1 C rates might be attributed to direct exposure to electrolyte components, leading to irreversible reactions. The initial discharge and charge capacity fading of bare $\alpha\text{-Fe}_2\text{O}_3$ electrode in the first and second cycle at 0.1 C-rate is ~479 and 116 mAh g^{-1} , respectively, while at 1 C-rate, it is about 397 mAh g^{-1} and 94 mAh g^{-1} , respectively. The rapid initial decrease in discharge specific capacity of the bare $\alpha\text{-Fe}_2\text{O}_3$

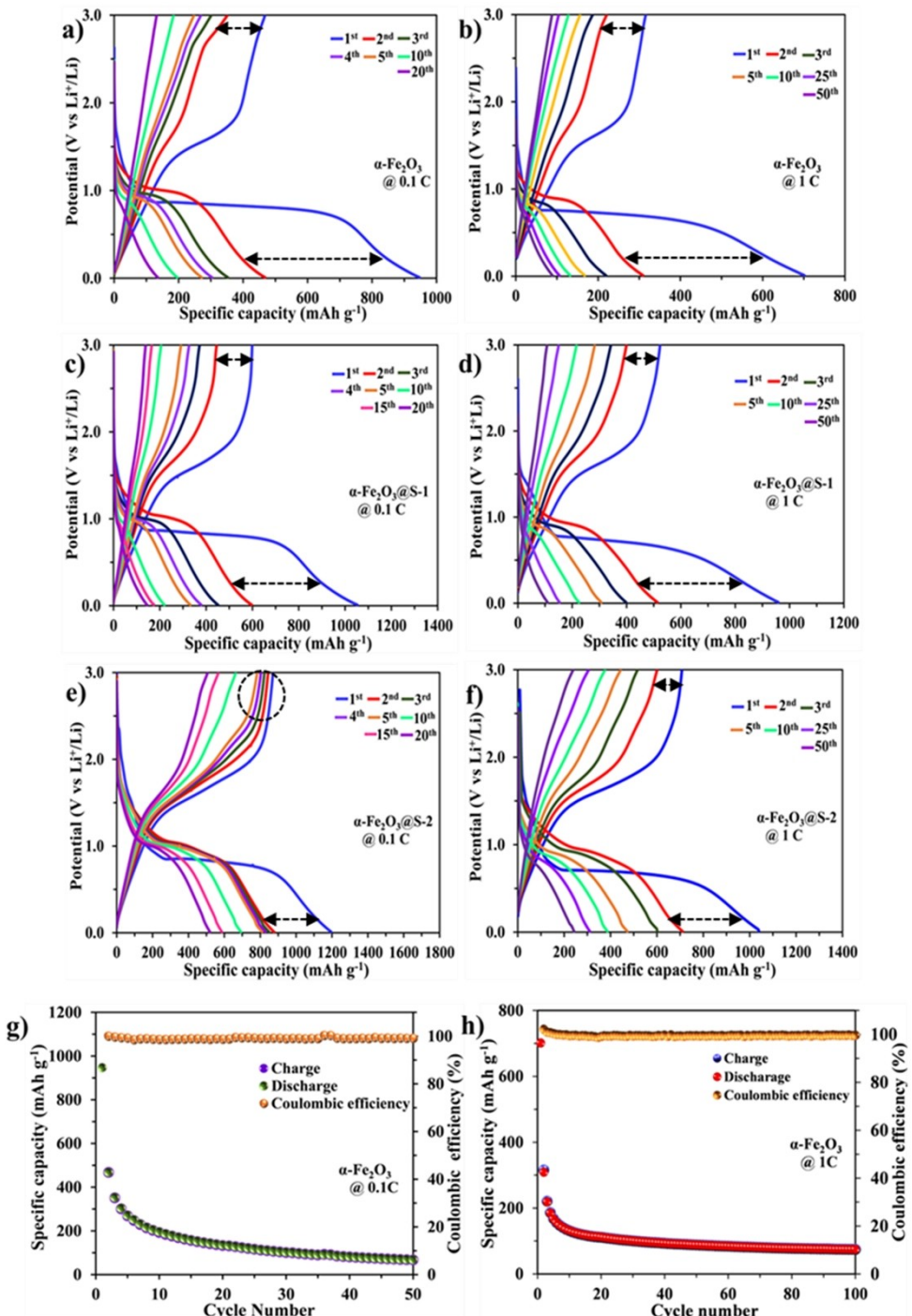


Figure 5. GCD curves of $\alpha\text{-Fe}_2\text{O}_3$, $\alpha\text{-Fe}_2\text{O}_3@\text{S-1}$, and $\alpha\text{-Fe}_2\text{O}_3@\text{S-2}$. a) GCD curve of bare $\alpha\text{-Fe}_2\text{O}_3$ at 0.1 C for 20 cycles vs Li⁺/Li. Charge-discharge profile of LIB with (c) $\alpha\text{-Fe}_2\text{O}_3@\text{S-1}$ at 0.1 C rate for 20 cycles, d) $\alpha\text{-Fe}_2\text{O}_3@\text{S-1}$ at 1 C rate for 50 cycles vs Li⁺/Li. GCD profile of LIB with (e) $\alpha\text{-Fe}_2\text{O}_3@\text{S-2}$ at 0.1 C rate for 20 cycles, f) $\alpha\text{-Fe}_2\text{O}_3@\text{S-2}$ at 1 C rate for 50 cycles vs Li⁺/Li at 1 C rate. Cyclic performance of LIB with (g) bare $\alpha\text{-Fe}_2\text{O}_3$ vs Li⁺/Li up to 50 cycles at 0.1 C, and (h) bare $\alpha\text{-Fe}_2\text{O}_3$ versus Li⁺/Li up to 100 cycles at 1 C.

electrode might be due to the consumption of lithium through reactions with surface oxygen in the bare $\alpha\text{-Fe}_2\text{O}_3$ electrode, resulting in the formation of an irreversible passive SEI layer at the electrode-electrolyte interface. Upon continued cycling, the specific discharge capacities of the bare $\alpha\text{-Fe}_2\text{O}_3$ electrode gradually decreased to 134 mAh g⁻¹ at 0.1 C rate at 20th cycle and 88 mAh g⁻¹ at 1 C-rate in the 50th cycle. Figure 5(c and d)

illustrates the GCD charge/discharge profile of sulfur-coated $\alpha\text{-Fe}_2\text{O}_3@\text{S-1}$ nanosheet over 20 and 50 cycles, at a constant current rate of 0.1 C and 1 C-rate respectively, spanning a potential range from 0.0 to 3.0 V. Initially, the $\alpha\text{-Fe}_2\text{O}_3@\text{S-1}$ electrode exhibits a discharge capacity of 1051 mAh g⁻¹ at a 0.1 C-rate, showing distinct discharge plateaus at 1.6, 1.55, and 0.9 V. The dual cathodic plateaus observed at 1.55 and 1.6 V are

corresponding to the active Li_xSO_y -based SEI layer formation and initial intercalation of Li^+ into the $\alpha\text{-Fe}_2\text{O}_3@\text{S-1}$ electrode corresponding to the reduction of Fe^{3+} to Fe^{2+} followed by the reversible $\text{Li}_2\text{Fe}_2\text{O}_3$ formation. As discussed earlier, the plateau observed at 0.9 V might be due to the reduction of Fe^{2+} to Fe^0 leading to the conversion reaction. Additionally, a subsequent cathodic peak is observed at 0.7 V, which may be attributed to the passive SEI layer formation due to the reduction of Li^+ ions with surface-adsorbed air molecules. Upon further charge-discharge cycles, due to the stable SEI formation, the plateau region 0.7 V disappeared. In this context, the surface-coated sulfur acts as a barrier, preventing direct contact between the active material and the electrolyte. This could be the reason for alleviating the formation of the irreversible SEI formation and electrolyte decomposition as evidenced by CV analysis. Furthermore, at 1 C-rate, the initial discharge capacity of the $\alpha\text{-Fe}_2\text{O}_3@\text{S-1}$ electrode is 958 mAh g^{-1} , with discharge plateaus observed at 1.2, 1.44, and 0.7 V as shown Figure 5d. These cathodic plateaus are indicative of the rapid reduction of Fe^{3+} to Fe^0 , driven by the swift lithium-ion kinetics at 1 C-rate. During the second discharge cycle, the $\alpha\text{-Fe}_2\text{O}_3@\text{S-1}$ electrode delivers a specific discharge capacity of 600 mAh g^{-1} at 0.1 C and 513 mAh g^{-1} for 1 C-rate. In the initial cycle, the charge-specific capacity of the $\alpha\text{-Fe}_2\text{O}_3@\text{S-1}$ electrode is 598 mAh g^{-1} for 0.1 C and 399 mAh g^{-1} at 1 C rate. Compared to the bare $\alpha\text{-Fe}_2\text{O}_3$ electrode, a substantial reduction in ICF is observed in the sulfur-coated $\alpha\text{-Fe}_2\text{O}_3@\text{S-1}$ electrode, both at a constant 0.1 C and under fast lithium-ion kinetics at 1 C. The initial discharge capacity fading of $\alpha\text{-Fe}_2\text{O}_3@\text{S-1}$ electrode during the first and second cycles at 0.1 C-rate is ~ 451 and 154 mAh g^{-1} , respectively. Upon further cycling, in the $\alpha\text{-Fe}_2\text{O}_3@\text{S-1}$ electrode, the specific discharge capacities gradually decrease to 143 mAh g^{-1} at 0.1 C rate for the 20th cycle and 108 mAh g^{-1} at 1 C rate for the 50th cycle.

Figure 5(e and f) describes the GCD profiles of sulfur-coated $\alpha\text{-Fe}_2\text{O}_3@\text{S-2}$ electrodes over 20 and 50 cycles, within the potential range of 0.0 to 3.0 V, at a constant current rate of 0.1 and 1 C-rate, respectively, in a coin-type half-cell. The $\alpha\text{-Fe}_2\text{O}_3@\text{S-2}$ electrode exhibits an initial discharge capacity of 1194 mAh g^{-1} at 0.1 C-rate (Figure 5e), with discharge plateaus observed at 2.34, 1.9, 1.63, and 0.8 V, respectively. The observed multiple cathodic plateaus resulted in the initial intercalation of Li^+ into the $\alpha\text{-Fe}_2\text{O}_3@\text{S-2}$ electrode, which might be attributed to an active Li_xSO_y -based SEI layer and lithium-ion intercalation from $\text{Li}_2\text{Fe}_2\text{O}_3$ as discussed in equation (1). This phenomenon is evidenced by CV curves for the $\alpha\text{-Fe}_2\text{O}_3@\text{S-2}$ electrode material vs. Li^+/Li . The elegant sulfur coating on the $\alpha\text{-Fe}_2\text{O}_3$ nanosheet as evidenced from HR-TEM analysis facilitates lithium-ion migration across the sulfur-coated $\alpha\text{-Fe}_2\text{O}_3$ nanosheet. The $\alpha\text{-Fe}_2\text{O}_3$ material, with its large surface area and homogeneous structure for lithium storage oxygen defect and the anionic sulfur-coated outer layer, provides more sites for Li^+ ion transport and storage. As a result, it exhibits an initially high specific discharge capacity compared to the bare and sulfur-coated $\alpha\text{-Fe}_2\text{O}_3@\text{S-1}$ electrode. Furthermore, a subsequent cathodic plateau observed at 0.68 V is predominantly, corresponding to the reduction of Fe^{3+} to Fe^0 which leads to the

conversion reaction as discussed earlier. In the case of the $\alpha\text{-Fe}_2\text{O}_3@\text{S-2}$ electrode, the ICF is significantly lower at both 0.1 C and 1 C rates which might be due to the Li-S based protective SEI layer formation on the surface of electrode, which inhibits direct contact between the electrode and the electrolyte. This development of Li_xSO_y active SEI layer formation circumvents the electrolyte decomposition followed by passive Li_2O -based SEI layer formation.

It's interesting to note that the initial discharge capacity of 946 mAh/g observed for bare $\alpha\text{-Fe}_2\text{O}_3$ electrode is close to the theoretical capacity of 1007 mAh/g. In the case of $\alpha\text{-Fe}_2\text{O}_3@\text{S-1}$ and $\alpha\text{-Fe}_2\text{O}_3@\text{S-2}$ electrodes, the initial discharge capacities are observed as 1051 and 1194 mAh/g, respectively which is higher than the theoretical capacity. This peculiar behaviour of hike in initial discharge capacity in sulfur coated $\alpha\text{-Fe}_2\text{O}_3@\text{S-1}$ and $\alpha\text{-Fe}_2\text{O}_3@\text{S-2}$ conversion electrodes might be due to the association of 6 Li^+ ions per molecule during the initial discharge cycle through conversion reaction mechanism as demonstrated in equations (1 to 4) which is in addition with SEI as well as FeS/FeS_2 contributions as discussed above. In closer observation of irreversible capacity and consumption of lithium-ions towards the formation of stable SEI layer in addition to the contribution through conversion reaction mechanism unambiguously clarifies the fact of hike in initial discharge capacity. In all these bare and sulfur coated $\alpha\text{-Fe}_2\text{O}_3$ electrodes, irreversible capacity loss of 50.7% (bare $\alpha\text{-Fe}_2\text{O}_3$), 43% (S1), and 27.1% (S2) are observed which might be due to the SEI layer formation. In the case of bare $\alpha\text{-Fe}_2\text{O}_3$ electrode, the formation of passive SEI layer leads to the consumption of huge lithium-ions during the initial discharge cycle as reflected in the 50.7% huge irreversible capacity loss. A similar but slightly contrast behaviour is also observed in S1 and S2 electrodes in which the consumption of lithium-ions towards the formation of stable as well as an active SEI layer contributed to the high discharge capacity. It's interesting to note that the irreversible capacity loss for S1 and S2 electrodes are much reduced while compared to that of bare $\alpha\text{-Fe}_2\text{O}_3$ electrode which might be due to the active SEI layer (i.e., Li_xSO_y) formation in S1 and S2 electrodes as discussed above. A detailed literature survey of Fe_2O_3 and other conversion electrode initial discharge capacity responses are included in Table S1 which clearly indicates that in most of the conversion electrodes, the initial discharge capacity is higher than the theoretical capacity. The reason for the huge initial discharge capacity in those reported literatures for Fe_2O_3 and other conversion electrodes had been interpreted in relation with the consumption of lithium-ions towards SEI formation at the first discharge. However, in most of the reports, drastic capacity fading have also been reported which are found to be huge in comparison with the studied S1 and S2 samples. In the present study, the physical and microwave treated approach of sulfur coating contributed to active SEI layer formation that very well controls and alleviates further capacity fading as evidenced from the cycling response. In the exceptional S2 electrode, the irreversible capacity loss after five cycles is found to be only 3.4% which indicates the effectiveness of active SEI layer that alleviates further pile up of SEI layer.

In addition to SEI contribution, the FeS/FeS₂ phase formation as a thin surface interfacial layer between Fe₂O₃/Sulfur in the sulfur coated electrodes is also contributing to the discharge capacity. The Fe₂O₃ particle might be covered by FeS/FeS₂ phase as an interface wrapping between top surface of Fe₂O₃ and inner spherical coverage of sulfur coating as evidenced from XRD as well as XPS results. The existence of FeS/FeS₂ phase is well reflected in CV results as well that could also be contributing through conversion reactions to the hike in discharge capacity as discussed in CV interpretation. The sulfur coating in S1 and S2 also contributes more active sites for additional storage of lithium-ions.

In nutshell, the increase in initial discharge capacity than the theoretical capacity might be due to the accommodation of large number of lithium ions by the α -Fe₂O₃ electrode through conversion reaction, consumption of much lithium-ions towards the formation of active SEI layer, and contribution from FeS/FeS₂ particle interface (i.e., Fe₂O₃/Sulfur) conversion component. These synergistic effects yielded in high initial discharge capacity for the S1 and S2 conversion type sulfur coated α -Fe₂O₃ electrodes.

Moreover, at 1 C-rate, the initial discharge capacity of the α -Fe₂O₃@S-2 electrode is 1039 mAh g⁻¹, with distinct discharge plateaus observed at 1.6, 1.5, and 0.7 V as shown in Figure 5f. These cathodic plateaus indicate the formation of SEI layer and the rapid reduction of Fe³⁺ to Fe⁰ as discussed earlier. Subsequent cycles reveal a coupled cathodic plateau at 1.6 and ~0.83 V, along with anodic peaks at 1.8 V and ~2.4 V, corresponding to the redox properties of the α -Fe₂O₃@S-2 electrode. During the initial cycle, the specific charge capacity of the α -Fe₂O₃@S-2 electrode is 871 mAh g⁻¹ at 0.1 C and 707 mAh g⁻¹ at 1 C rate. In the second discharge cycle, the α -Fe₂O₃@S-2 electrode delivers a specific discharge capacity of 877 mAh g⁻¹ at 0.1 C and 710 mAh g⁻¹ for 1 C-rate. Compared to the bare α -Fe₂O₃ and α -Fe₂O₃@S-1 electrodes, a significant reduction in ICF is observed in the sulfur-coated α -Fe₂O₃@S-2 electrode, both at a constant 0.1 C as well as at 1 C rate. The initial discharge capacity fading of the α -Fe₂O₃@S-2 electrode during the first and second cycles at 0.1 C-rate is ~317 and 329 mAh g⁻¹, respectively, and the initial charge capacity fading of the same electrode in the first and second charge cycles is 28 mAh g⁻¹ at 0.1 C-rate. Compared to all the electrodes, the sulfur-coated α -Fe₂O₃@S-2 electrodes exhibit very low ICF at 0.1 C and 1 C-rate due to the active Li_xSO_y-SEI layer formation. In both the bare and sulfur coated α -Fe₂O₃@S-1 and α -Fe₂O₃@S-2 electrodes, there is ample time for electrochemical alterations to occur due to the slow kinetics at 0.1 C-rate, resulting in relatively higher discharge capacities compared to the kinetics at 1 C-rate. Upon further cycling, the specific discharge capacities of the α -Fe₂O₃@S-2 electrode gradually decrease to 518 mAh g⁻¹ at 0.1 C for the 20th cycle and 247 mAh g⁻¹ at 1 C-rate for the 50th cycle. The charge-specific capacity of the α -Fe₂O₃@S-2 electrode, produced through a physical method followed by microwave-assisted treatment with sulfur (α -Fe₂O₃@S-2), is notably superior to that of the bare and α -Fe₂O₃@S-1 synthesized by using a physical method followed by calcination. This improvement may be attributed to the even

surface coating of sulfur on α -Fe₂O₃ as evidenced from HR-TEM analysis. A comprehensive review of the literature (Table S2) comparing the discharge capacity of bare and sulfur coated α -Fe₂O₃ electrodes reveals that the currently examined bare and sulfur coated α -Fe₂O₃ electrodes demonstrate relatively better electrochemical performance.

Figure 5(g and h) shows the specific capacity and Columbic Efficiency (CE) of bare α -Fe₂O₃ electrode as a function of a number of cycles, specifically 50 cycles at 0.1 C rate and 100 cycles at 1 C rate. The initial discharge capacity of the bare α -Fe₂O₃ electrode at 0.1 C-rate is found to be 946 mAh g⁻¹ with a coulombic efficiency of 96%, whereas at 1 C rate, the discharge capacity is 701 mAh g⁻¹. The substantial initial discharge capacity during the initial cycle is attributed to the significant consumption of lithium ions for forming the SEI layer on the surface of the bare α -Fe₂O₃ electrode. Upon prolonged cycling, the discharge capacity moderately decreases to 68.3 mAh g⁻¹ by the 50th cycle for bare α -Fe₂O₃ electrode while maintaining a 100% Coulombic efficiency at 0.1 C-rate. At a 1 C-rate, the discharge capacity of bare α -Fe₂O₃ electrode progressively diminishes to 75 mAh g⁻¹ at the 100th cycle with a CE of about 99.6%. The gradual decline in capacity observed in α -Fe₂O₃ electrodes from the 2nd cycle onwards, both at 0.1 C and 1 C rates, may be attributed to the continuous pile-up of intermetallic compounds such as Li₂CO₃ and Li₂O as thick SEI layer formation on the electrode surface due to the free radical components from the gradual decomposition of the electrolyte.

Figure 6(a and b) depict the specific capacity and CE against the number of cycles for sulfur-coated α -Fe₂O₃@S-1 electrodes with 50 cycles at a constant current of 0.1 C and 200 cycles at a 1 C-rate. The initial discharge capacity of the sulfur-coated α -Fe₂O₃@S-1 electrode at 0.1 C-rate is 1051 mAh g⁻¹, accompanied by a Coulombic efficiency of 97%. At a 1 C-rate, the discharge capacity is 958 mAh g⁻¹ with a Coulombic efficiency of about ~98%. Notably, the sulfur-coated α -Fe₂O₃@S-1 electrode exhibits reduced initial discharge capacity fading compared to the bare α -Fe₂O₃ electrode. This might be attributed to forming the active Li_xSO_y-SEI layer during the initial discharge processes which minimizes undesired irreversible reactions leading to Li₂O formation.

The surface-coated Li-S based SEI layer prevents electrode rupture and unwanted reactions between electrolyte components and the active electrode material. As previously discussed, a substantial amount of lithium-ion is consumed during the initial discharge for SEI layer formation in α -Fe₂O₃@S-1 electrode. Upon continuous cycling, the discharge capacity gradually diminishes to 69 mAh g⁻¹ for the 50th cycle at 0.1 C-rate and 56 mAh g⁻¹ for the 200th cycle at a 1 C-rate while maintaining a CE of 100%. Interestingly, it is worth noting that during further cycles in α -Fe₂O₃@S-1 electrodes at 1 C-rate (indicative of fast lithium-ion kinetics), very stable discharge capacity is observed, with a consistent value of 56 mAh g⁻¹ from 130th to 200th cycle. Thus, in α -Fe₂O₃@S-1 electrodes at a 1 C-rate, the discharge capacity remains stable at 56 mAh g⁻¹ with 100% Coulombic efficiency retention up to the 200th cycle. Figure 6(c and d) depicts the specific charge-discharge capacity and columbic efficiency plotted against the number of cycles for sulfur-coated

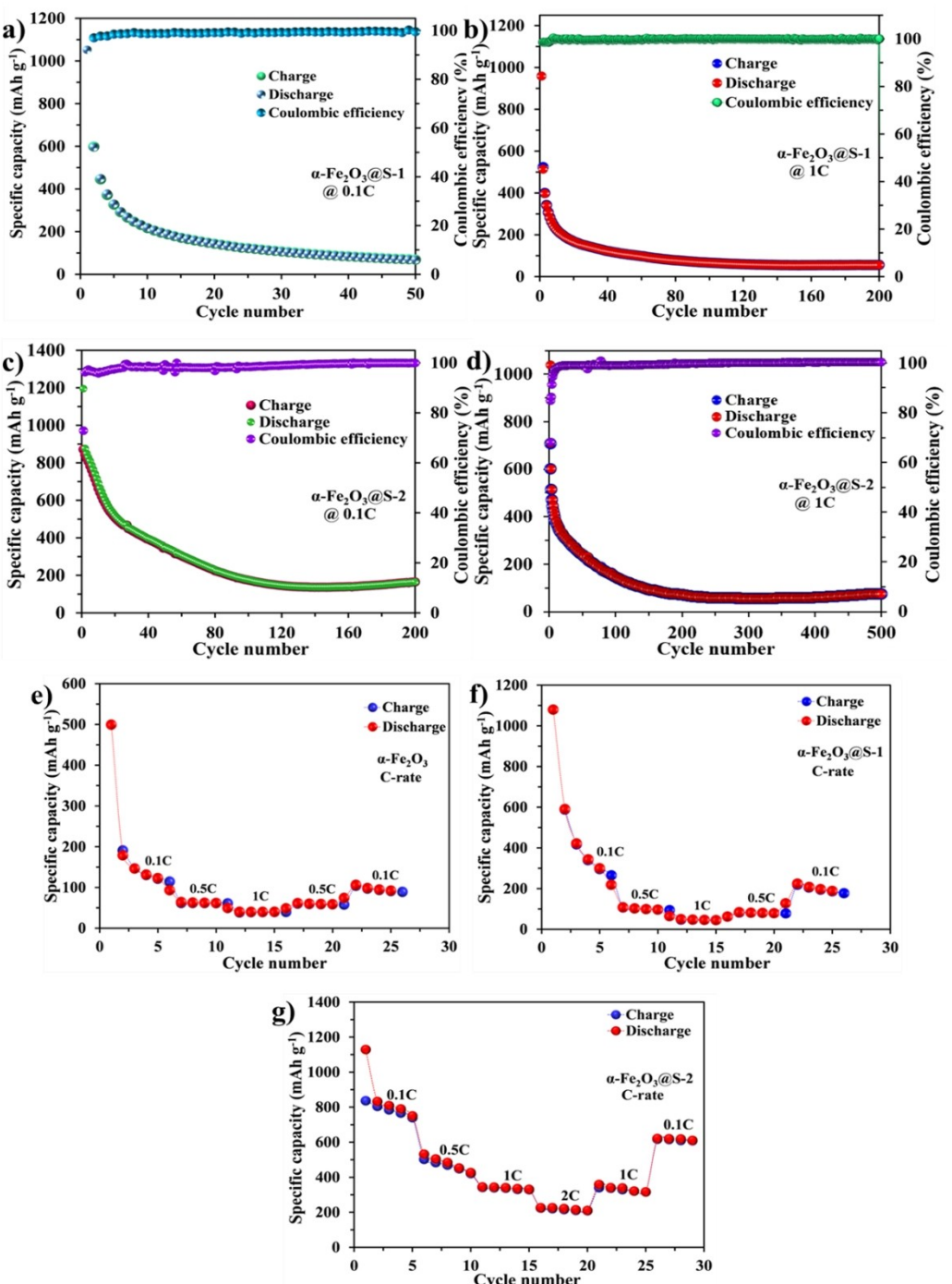


Figure 6. Cyclic performance of LIB with (a) $\alpha\text{-Fe}_2\text{O}_3\text{@S-1}$ versus Li⁺/Li up to 50 cycles at 0.1 C and b) $\alpha\text{-Fe}_2\text{O}_3\text{@S-1}$ vs Li⁺/Li up to 200 cycles at 1 C. c) Cyclic performance of $\alpha\text{-Fe}_2\text{O}_3\text{@S-2}$ versus Li⁺/Li up to 200 cycles at 0.1 C. d) $\alpha\text{-Fe}_2\text{O}_3\text{@S-2}$ vs Li⁺/Li up to 500 cycles at 1 C. C-rate performance of LIB with (e) bare $\alpha\text{-Fe}_2\text{O}_3$ vs Li⁺/Li at different current densities. f) C-rate performance of $\alpha\text{-Fe}_2\text{O}_3\text{@S-1}$ versus Li⁺/Li at different current densities. g) C-rate performance of $\alpha\text{-Fe}_2\text{O}_3\text{@S-2}$ versus Li⁺/Li at different current densities.

$\alpha\text{-Fe}_2\text{O}_3\text{@S-2}$ electrodes. The cyclic response of $\alpha\text{-Fe}_2\text{O}_3\text{@S-2}$ electrodes performed for 200 cycles at 0.1 C rate is shown in Figure 6(c), and for 500 cycles at 1 C rate is shown in Figure 6(d). The $\alpha\text{-Fe}_2\text{O}_3\text{@S-2}$ electrode exhibits an initial discharge capacity of 1194 mAh g⁻¹ with a coulombic efficiency of 72% at 0.1 C. Furthermore, at a 1 C-rate, it achieves 1039 mAh g⁻¹ with a CE of ~70% retention. Notably, the $\alpha\text{-Fe}_2\text{O}_3\text{@S-2}$ electrode demon-

strates minimal initial discharge capacity fading compared to the bare and sulfur-coated $\alpha\text{-Fe}_2\text{O}_3\text{@S-1}$ electrodes, both 0.1 C and 1 C-rates, as shown in Figure 6(c and d). This phenomenon may be attributed to the forming of an active Li_xSO_y-based-SEI layer during the initial discharge processes, which mitigates unwanted irreversible reactions involving the reduction of lithium-ion with surface adsorbed air molecules and electrolyte

decomposed components at the electrode-electrolyte interface. This proves that the surface-coated Li_xSO_y -based-SEI layer acts as a lithium-ion transport medium, facilitating ion movement in both slow and fast lithium-ion kinetics at 0.1 C and the high 1 C rate, respectively. The sulfur coating on $\alpha\text{-Fe}_2\text{O}_3$ also prevents the active material from rupturing and also avoiding direct contact with the electrolyte leads to the irreversible intermetallic compound formation. During initial redox process, a significant amount of lithium-ion is expended to form a smooth Li_xSO_y -based SEI layer on the surface of the $\alpha\text{-Fe}_2\text{O}_3@\text{S-2}$ electrode. In addition, a plausible pathway for lithium-ion migration through sulfur might be established via electrochemical alteration, which could contribute to the rapid increase in charge-discharge specific capacity as observed in sulfur-coated $\alpha\text{-Fe}_2\text{O}_3@\text{S-2}$ electrode at 0.1 C and 1 C-rate. Notably, while cycling, the discharge capacity rapidly increases from 145 mAh g^{-1} at the 120th cycle to 165 mAh g^{-1} at the 200th cycle at 0.1 C-rate, with a coulombic efficiency of 99.5% respectively. However, it is interesting to observe that with further cycling in $\alpha\text{-Fe}_2\text{O}_3@\text{S-2}$ electrodes at 1 C-rate (indicating fast lithium-ion kinetics), the specific charge-discharge capacity rapidly increases from 71 mAh g^{-1} at the 200th to 76 mAh g^{-1} at the 500th cycle, while maintaining a coulombic efficiency of about 99.5%. The C-rate performance of bare $\alpha\text{-Fe}_2\text{O}_3$ electrode vs Li^+/Li at various current densities is depicted in Figure 6(e) and exhibits a descending step-like behaviour in the discharge-specific capacity as current densities increase. At 0.1 C, the bare $\alpha\text{-Fe}_2\text{O}_3$ electrode delivers a discharge capacity of 499 mAh g^{-1} , which decreases to 48 mAh g^{-1} at a 1 C rate. The discharge capacity remains low at a higher C-rate (1 C). However, there is an immediate increase in discharge capacity to a steady value of 74 mAh g^{-1} when the C rate is decreased to 0.5 C. When the current density is reduced from 0.5 C to 0.1 C rate, the $\alpha\text{-Fe}_2\text{O}_3$ electrode exhibits a discharge capacity 106 mAh g^{-1} . The low discharge capacity observed at high C-rate might be due to the restricted lithium-ion redox reaction. In the sulfur-coated $\alpha\text{-Fe}_2\text{O}_3$ electrode, the discharge capacity is 1079 mAh g^{-1} at 0.1 C rate which drops to 50 mAh g^{-1} at 1 C-rate as shown in Figure 6(f). When the current density suddenly decreases from higher C-rate to 0.1 C-rate, the discharge capacity increases to 224 mAh g^{-1} . Figure 6(g) illustrates the C-rate performance of sulfur-coated $\alpha\text{-Fe}_2\text{O}_3@\text{S-2}$ electrode versus Li^+/Li at various current densities. As the current density increases, a descending step-like behaviour in discharge-specific capacity is observed in the $\alpha\text{-Fe}_2\text{O}_3@\text{S-2}$ electrode. The initial discharge of the $\alpha\text{-Fe}_2\text{O}_3@\text{S-2}$ electrode delivers 1128 mAh g^{-1} at 0.1 C-rate, which drops to 225 mAh g^{-1} at 2 C-rate. Compared to bare and sulfur coated $\alpha\text{-Fe}_2\text{O}_3@\text{S-1}$ electrodes, the microwave assisted sulfur coated $\alpha\text{-Fe}_2\text{O}_3@\text{S-2}$ electrode tends to perform well at high current densities, particularly at 2 C-rate. This behaviour may be attributed to the formation of a smooth Li_xSO_y active SEI layer on the surface of the electrode as discussed earlier. When the current density gradually decreases from 2 C to 0.1 C-rate, the $\alpha\text{-Fe}_2\text{O}_3@\text{S-2}$ electrode delivers a discharge capacity of 620 mAh g^{-1} . This excellent C-rate capability might be due to the active Li_xSO_y based SEI layer formation on the surface of electrode as discussed earlier. The Electrochemical Impedance

Spectroscopy of bare- $\alpha\text{-Fe}_2\text{O}_3$, $\alpha\text{-Fe}_2\text{O}_3@\text{S-1}$ and $\alpha\text{-Fe}_2\text{O}_3@\text{S-2}$ electrodes before and after cycles are shown in Figure S5 Supplementary Information with a detailed analysis. The EIS results reveal that the sulfur coating expedite lithium-ion kinetics across the interface and enhances the electrochemical performance.

Figure 7(a) shows the discharge-specific capacity and working voltage versus the number of cycles for the bare $\alpha\text{-Fe}_2\text{O}_3$ electrode at 1 C-rate. Initially, the working voltage of the $\alpha\text{-Fe}_2\text{O}_3$ electrode is 0.9 V, but after a few cycles, it decreases to 0.8 V. By the 100th cycle, the working potential of the bare $\alpha\text{-Fe}_2\text{O}_3$ electrode reaches 0.7 V versus Li^+/Li . As previously discussed, this decline in working voltage may be attributed to the irreversible reaction of Li_2O on the electrode's surface and direct contact between the electrode and the electrolyte. The average energy density of the $\alpha\text{-Fe}_2\text{O}_3$ electrode is ~81 Wh/kg for 100 cycles at 1 C-rate. In Figure 7(b) the discharge capacity working potential versus cycle number of the $\alpha\text{-Fe}_2\text{O}_3@\text{S-1}$ electrode vs Li^+/Li is displayed. The $\alpha\text{-Fe}_2\text{O}_3@\text{S-1}$ electrode exhibits a working potential of 0.9 V in the first few cycles. As the cycling progress, the working voltage stabilizes at 0.8 V and eventually reaches 1.0 V by the 200th cycle. The average energy density of the sulfur-coated $\alpha\text{-Fe}_2\text{O}_3@\text{S-1}$ electrode is ~116 Wh/kg after 100 cycles and ~84 Wh/kg after 200 cycles at 1 C-rate. Similarly, Figure 7(c) illustrates the discharge capacity and working potential versus cycle number of the $\alpha\text{-Fe}_2\text{O}_3@\text{S-2}$ electrode versus Li^+/Li . The $\alpha\text{-Fe}_2\text{O}_3@\text{S-2}$ electrode initially exhibits a working potential of 0.9 V in early cycles, which subsequently varies between 0.8 V and 0.7 V. This variation may be attributed to the stabilization processes of the SEI layer, with the final working voltage reaching 0.93 V by the 500th cycles. Compared to bare and $\alpha\text{-Fe}_2\text{O}_3@\text{S-1}$ electrodes, the sulfur-coated $\alpha\text{-Fe}_2\text{O}_3@\text{S-2}$ electrode delivers the highest average energy density of ~246 Wh/kg up to 100 cycles and ~97 Wh/kg up to 500 cycles at 1 C-rate.

The energy density increment of $\alpha\text{-Fe}_2\text{O}_3@\text{S-1}$ and $\alpha\text{-Fe}_2\text{O}_3@\text{S-2}$ electrodes might be due to the large amount of lithium-ion storage in S1 and S2 electrodes compared to bare $\alpha\text{-Fe}_2\text{O}_3$ electrode. Especially, the elegant sulfur coating on the $\alpha\text{-Fe}_2\text{O}_3$ prevents direct contact between the electrode and electrolyte by the formation of an active Li_2SO_4 based SEI layer which effectively facilitates ionic diffusion kinetics across the interface. In addition, the active layer prevents electrolyte degradation by cutting off any unwanted side reactions which enhances the specific capacity as well as the working potential of the electrode.

In the sulfur coated $\alpha\text{-Fe}_2\text{O}_3$ samples, the band gap of the $\alpha\text{-Fe}_2\text{O}_3$ would have dramatically reduced from 2.3 eV to 1.18 eV^[73] which contributes to the increase in electronic conductivity of $\alpha\text{-Fe}_2\text{O}_3@\text{S-1}$ and $\alpha\text{-Fe}_2\text{O}_3@\text{S-2}$ electrodes. The increased electronic conductivity facilitates better electron flow during redox reactions in the S1 and S2 anode samples. The S1 and S2 electrodes can effectively store and release more Li-ions during the discharge-charge process due to the conversion reaction, protected electrode surface, and facile charge transfer kinetics across the interface which enhances energy stored per gram in S1 and S2 electrodes that resulted in increased energy

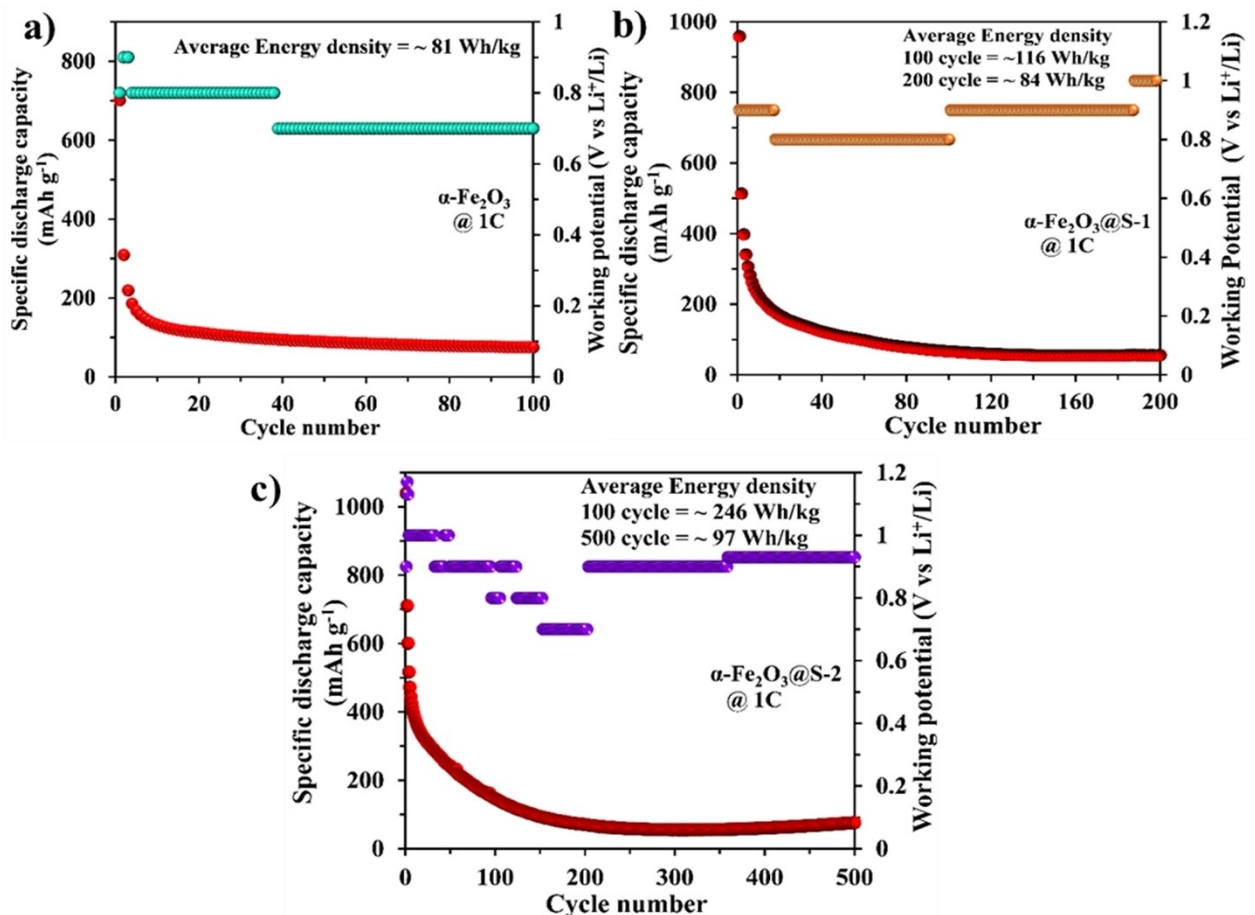


Figure 7. Specific discharge capacity, working potential variations with respect to cycle number for a) bare $\alpha\text{-Fe}_2\text{O}_3$ vs Li^+/Li up to 100 cycles at 1 C-rate. b) $\alpha\text{-Fe}_2\text{O}_3@\text{S-1}$ up to 200 cycles at 1 C-rate, and c) $\alpha\text{-Fe}_2\text{O}_3@\text{S-2}$ electrode vs Li^+/Li up to 500 cycles at 1 C-rate.

density. In the case of bare $\alpha\text{-Fe}_2\text{O}_3$ electrode, the direct contact between the electrode and electrolyte surface leads to unwanted side reactions such as Li_2O formation and electrolyte degradation which reduces the working potential and leading to initial capacity fading, causes the low energy density and specific capacity of the bare $\alpha\text{-Fe}_2\text{O}_3$ during cycling.

In order to gain a better understanding of lithium-ion kinetics, an in-situ galvanostatic intermittent titration technique (GITT) for the evaluation of lithium-ion diffusion coefficient (D_{Li^+}) has been performed on the bare $\alpha\text{-Fe}_2\text{O}_3$ and sulfur-coated $\alpha\text{-Fe}_2\text{O}_3@\text{S-1}$ and $\alpha\text{-Fe}_2\text{O}_3@\text{S-2}$ electrodes during discharge-charge measurements shown in Figure 8(a-f). The GITT performance of all the electrodes is performed in the potential range of 0.0 to 3.0 V, with a time interval of 15 minutes for all the electrodes at 0.1 C-rate and the results are depicted in Figure 8(a,c,e). The GITT profiles for these electrodes indicate distinct charge-discharge plateaus occurring at different voltages vs. Li^+/Li . Notably, the sulfur-coated $\alpha\text{-Fe}_2\text{O}_3@\text{S-2}$ electrode exhibits prominent plateaus at various states of charge and discharge (SOC) compared to Li^+/Li .

The calculation of (D_{Li^+}) is carried out by using a simplified version of Fick's second law, involving a series of reasonable empirical evidence and computations. Based on the GITT curves, the Lithium ion diffusion co-efficient (D_{Li^+}) of the $\alpha\text{-Fe}_2\text{O}_3$

based working electrodes could be calculated by using the following equation.^[74,75]

$$D_{\text{Li}^+} = \frac{4}{\pi\tau} \left(\frac{m_B V_M}{M_B S} \right)^2 \left(\frac{\Delta E_s}{\Delta E_\tau} \right)^2 (\tau \ll L^2/D_{\text{Li}^+}) \quad (7)$$

where (V_M) is the effective materials molar volume ($\text{cm}^3\text{mol}^{-1}$), ' M_B ' is the molecular weight of the material (g mol^{-1}), ' m_B ' denotes the mass of the effective materials in an electrode (g), ' τ' is the constant current pulse duration time (s), 'S' is the surface area of the electrode (cm^2), ' ΔE_τ ' is total voltage changes during the current pulse while neglecting the 'iR' drop (V) and ' ΔE_s ' is the change in steady-state voltage during constant current titration (V). Figure 8(b,d,f) shows the calculated lithium diffusion coefficient (D_{Li^+}) values for all three electrodes at various SOC (%). During the discharge process, the D_{Li^+} value for the bare- $\alpha\text{-Fe}_2\text{O}_3$ electrode varies in the range of $10^{-11}\text{--}10^{-10} \text{ cm}^2\text{s}^{-1}$, for sulfur-coated $\alpha\text{-Fe}_2\text{O}_3@\text{S-1}$, the lithium diffusion coefficient varies in the range of $10^{-12}\text{--}10^{-10} \text{ cm}^2\text{s}^{-1}$, and finally, the $\alpha\text{-Fe}_2\text{O}_3@\text{S-2}$ electrode delivers the D_{Li^+} Values vary from 10^{-13} to $10^{-10} \text{ cm}^2\text{s}^{-1}$. These values correspond to varying SOC (%) levels relative to their respective voltages. As shown in Figure 8(b), the entire lithium diffusion coefficient plots during the discharge process can be calculated in four

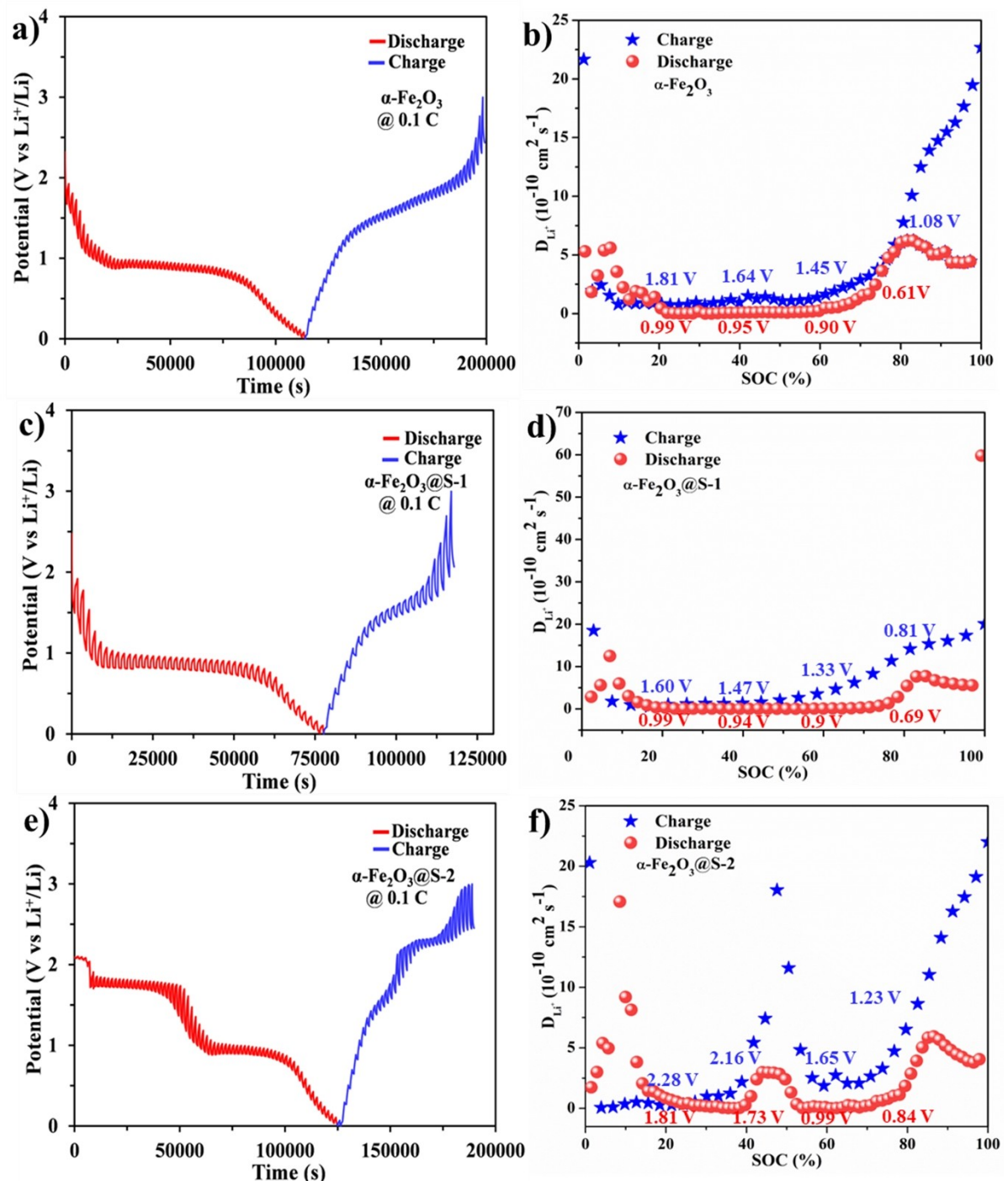


Figure 8. Galvanostatic Intermittent Titration Technique of as-synthesized bare and sulfur-coated electrodes. a) GITT plateau of bare $\alpha\text{-Fe}_2\text{O}_3$ Vs. Li^+/Li at 0.1 C-rate and b) the corresponding lithium diffusion co-efficient (D_{Li^+}) of bare $\alpha\text{-Fe}_2\text{O}_3$, c) GITT pattern of $\alpha\text{-Fe}_2\text{O}_3@\text{S-1}$ electrode at 0.1 C-rate, and d) the corresponding lithium-ion diffusion Co-efficient of $\alpha\text{-Fe}_2\text{O}_3@\text{S-1}$ electrode vs SOC. e) GITT pattern of the single discharge-charge cycle of $\alpha\text{-Fe}_2\text{O}_3@\text{S-2}$ electrode Vs. Li^+/Li , and f) the corresponding lithium diffusion coefficient (D_{Li^+}) of the $\alpha\text{-Fe}_2\text{O}_3@\text{S-2}$ electrode in the initial discharge-charge cycle at a current rate of 0.1 C.

different states of SOC (%) concerning their corresponding voltage (V). The calculated lithium diffusion coefficient (D_{Li^+}) of bare- $\alpha\text{-Fe}_2\text{O}_3$ electrode for 20%, 40%, 60% and 80% of SOC are found to be $D_{\text{Li}^+} = 4.63 \times 10^{-11} \text{ cm}^2 \text{s}^{-1}$ at 0.99 V, $1.05 \times 10^{-11} \text{ cm}^2 \text{s}^{-1}$ at 0.95 V, $2.41 \times 10^{-11} \text{ cm}^2 \text{s}^{-1}$ at 0.9 V and $6.04 \times 10^{-10} \text{ cm}^2 \text{s}^{-1}$ at 0.61 V, respectively. During the discharge

processes, the lithium diffusion coefficient is gradually increasing from 80 to 100% of SOC. During the initial charge cycle, the D_{Li^+} Value for the bare- $\alpha\text{-Fe}_2\text{O}_3$ electrode varies from 10^{-11} to $10^{-10} \text{ cm}^2 \text{s}^{-1}$. The lithium-ion diffusion co-efficient (D_{Li^+}) of sulfur-coated $\alpha\text{-Fe}_2\text{O}_3@\text{S-1}$ electrode during the initial discharge processes is calculated at various SOCs concerning to the

corresponding voltage. The calculated D_{Li^+} values of $\alpha\text{-Fe}_2\text{O}_3@\text{S-1}$ electrode indicates $2.83 \times 10^{-11} \text{ cm}^2 \text{s}^{-1}$ for 20% SOC, and $D_{Li^+} = 6.06 \times 10^{-12} \text{ cm}^2 \text{s}^{-1}$ for 40% of SOC, $8.05 \times 10^{-12} \text{ cm}^2 \text{s}^{-1}$ for 60% of SOC, and $5.43 \times 10^{-10} \text{ cm}^2 \text{s}^{-1}$ for 80% of SOC corresponding to the respective voltages at 0.99 V, 0.94, 0.90 and 0.69 V as shown in Figure 8(d). The lithium diffusion coefficient gradually increases from 80 to 100% of SOC during the discharge processes. The initial charge cycle of the $\alpha\text{-Fe}_2\text{O}_3@\text{S-1}$ electrode exhibits the D_{Li^+} in a wide range of 10^{-10} to $10^{-9} \text{ cm}^2 \text{s}^{-1}$. Figure 8(f) shows that the $\alpha\text{-Fe}_2\text{O}_3@\text{S-2}$ electrode exhibits multiple curves during the discharge cycle, which might be due to the initial lithium-ion intercalation with leads to the formation of a Li_xSO_y -based SEI layer on the surface of the electrode as discussed in CV results. The entire lithium diffusion coefficient (D_{Li^+}) of sulfur-coated $\alpha\text{-Fe}_2\text{O}_3@\text{S-2}$ electrode is calculated in four different SOC (%) states concerning the voltage (V). The calculated lithium diffusion coefficient (D_{Li^+}) values of $\alpha\text{-Fe}_2\text{O}_3@\text{S-2}$ electrode are found to be $8.55 \times 10^{-11} \text{ cm}^2 \text{s}^{-1}$ for 20% SOC at 1.81 V, $2.84 \times 10^{-11} \text{ cm}^2 \text{s}^{-1}$ for 40% SOC at 1.73 V, $3.97 \times 10^{-13} \text{ cm}^2 \text{s}^{-1}$ for 60% SOC at 0.99 V, and $2.87 \times 10^{-10} \text{ cm}^2 \text{s}^{-1}$ for 80% SOC at 0.84 V. The charge cycle of the $\alpha\text{-Fe}_2\text{O}_3@\text{S-2}$ electrode exhibits the D_{Li^+} varies in the range of 10^{-11} to $10^{-10} \text{ cm}^2 \text{s}^{-1}$. The lithium-ion diffusion coefficient of the $\alpha\text{-Fe}_2\text{O}_3@\text{S-2}$ electrode exhibits a slight fluctuation at the beginning of discharging which might be due to the lithium-ion polarization phenomenon that causes reaction kinetic with sulfur components for the formation of smooth Li_xSO_y -SEI. The sulfur-coated $\alpha\text{-Fe}_2\text{O}_3@\text{S-2}$ electrode delivers a higher ionic diffusion coefficient ($2.87 \times 10^{-10} \text{ cm}^2 \text{s}^{-1}$) than all the electrodes at 80% SOC which might be due to the active SEI layer formation and also supported by the presence of oxygen defects as evidenced from HRTEM and XPS results. The lithium-ion diffusion coefficient (D_{Li^+}) values of all the bare and sulfur coated $\alpha\text{-Fe}_2\text{O}_3$ electrodes during initial discharge-charge cycle are illustrated in (Table S3).

Figure S6(a–c) shows a single discharge curve with respect to time for all the samples which clearly exhibits a step like behaviour corresponding to SEI formation, different redox reactions in the respective samples. In the sulfur coated samples, an active Li_xSO_y based SEI layer is expected based on XRD, however understanding the formation of the SEI layer between the electrode and electrolyte and its impact is challenging. To comprehend the development of the SEI layer, an ex-situ HR-SEM cross-section (90°) and XRD analyses have been carried out. In most electrodes, SEI formation at the interface between the electrode and electrolyte is barrier to ion migration in the interfacial region. In this study, the SEI layer developed at the interface of the electrode-electrolyte especially for the sulfur coated $\alpha\text{-Fe}_2\text{O}_3$ electrodes contribute actively that facilitates lithium-ion migration into the electrode surface with negligible resistance.

The ex-situ study aims to find the elements in the SEI layer developed at the interface of the electrode-electrolyte for a single discharge cycle. The SEI layer compound formed in the case of sulfur coated $\alpha\text{-Fe}_2\text{O}_3$ samples are expected to be contributing efficiently to the ionic diffusion into the electrode surface. Understanding the SEI layer components and its

contributions is a tough task to be achieved. In an effort, bare and sulfur-coated $\alpha\text{-Fe}_2\text{O}_3@\text{S-1}$ and $\alpha\text{-Fe}_2\text{O}_3@\text{S-2}$ electrodes used for single discharge coin cells are taken for post-redox ex-situ evaluations. In order to carry out the XRD measurements, all the coin cells are dismantled, and the delicate electrodes are dried under an argon atmosphere, as explained in electrode fabrications of supporting information.

Figure 9(a) shows a steady mode ex-situ XRD pattern of bare $\alpha\text{-Fe}_2\text{O}_3$ (FB), sulfur-coated $\alpha\text{-Fe}_2\text{O}_3@\text{S-1}$ (FS-1), and $\alpha\text{-Fe}_2\text{O}_3@\text{S-2}$ (FS-2) electrodes exposed to a single discharge cycle. The strong, intense peaks observed in all the samples at 43.29°, 50.43°, and 74.13° are corresponding to the reflections from (111), (200), and (220) crystallographic planes which might be attributed to the copper substrate (ICDD card no: 00-004-0836).^[76,77] Since all the cells are dismantled at the discharge state, none of the electrode peaks are significant except the broad peak observed at 63.99° and 84.91° which are corresponding to the (300) and (134) crystallographic planes of bare $\alpha\text{-Fe}_2\text{O}_3$ electrode. In order to visualize the low angle reflection planes, the XRD plot is magnified in the 2θ range of 10° to 40°. The magnified XRD pattern indicates two slight humps at 64.5° and 85.2° in the FB and FS1 electrodes which are corresponding to the (300) and (134) reflection planes due to the rhombohedral phase of $\alpha\text{-Fe}_2\text{O}_3$ (ICDD: 00-033-0664).^[36–38] In the FB electrode, less intense peaks observed at 56.34°, 67.27°, and 83.83° are corresponding to (220), (311), and (400) reflection planes which might be due to the Li_2O cubic phase (ICDD card No: 00-012-0254).^[78] The formation of Li_2O in the FB electrode may be due to the capture of mobile lithium ions by oxygen anions arise from the decomposition of electrolyte components as well as surface-adsorbed oxygen of the electrode. Notably, no specific Li_2O peaks are observed in the FS-1 and FS-2 electrodes, which highly confirms the absence of Li_2O formation in both electrodes, resulting in only Li_xSO_y -based SEI layer formation in FS-1 and FS-2 electrodes. In the magnified XRD pattern of FS-1 and FS-2 electrodes, a few 2θ peaks appeared at 24.13°, 33.15°, and 35.61° are corresponding to the (012), (104), and (110) crystal planes of bare $\alpha\text{-Fe}_2\text{O}_3$ (ICDD No: 00-033-0664).^[36–38] In both FS-1 and FS-2 electrodes, the appearance of new significant (2θ) peaks observed at 32.0°, 33.20°, 33.26°, 37.40° and 38.80° are corresponding to (−212), (112), (211) (−311) and (−213) monoclinic phase of in-situ formed Li_2SO_4 SEI layer on the surface of FS-1 and FS-2 electrodes (ICDD No: 00-020-0640).^[79–82] The formation of Li_2SO_4 in the FS-1 and FS-2 electrodes might be due to a facile reaction between lithium cation and sulfur anion during the first discharge processes. In order to confirm the presence of Li_2SO_4 formation and to understand the composition of SEI layer, all the electrodes have been further investigated under ex-situ cross-section HR-SEM analysis associated with elemental mapping.

Figure 9(b) shows the HR-SEM cross-section image observed at 90° angle bare $\alpha\text{-Fe}_2\text{O}_3$ electrode subjected to a first discharge cycle. The cross-section image of the FB electrode indicates an irregular top SEI layer, which might be attributed to the formation of intermetallic lithium compounds, particularly Li_2O , as confirmed by ex-situ steady mode XRD analysis. On the other hand, for the FS-1 and FS-2 electrodes,

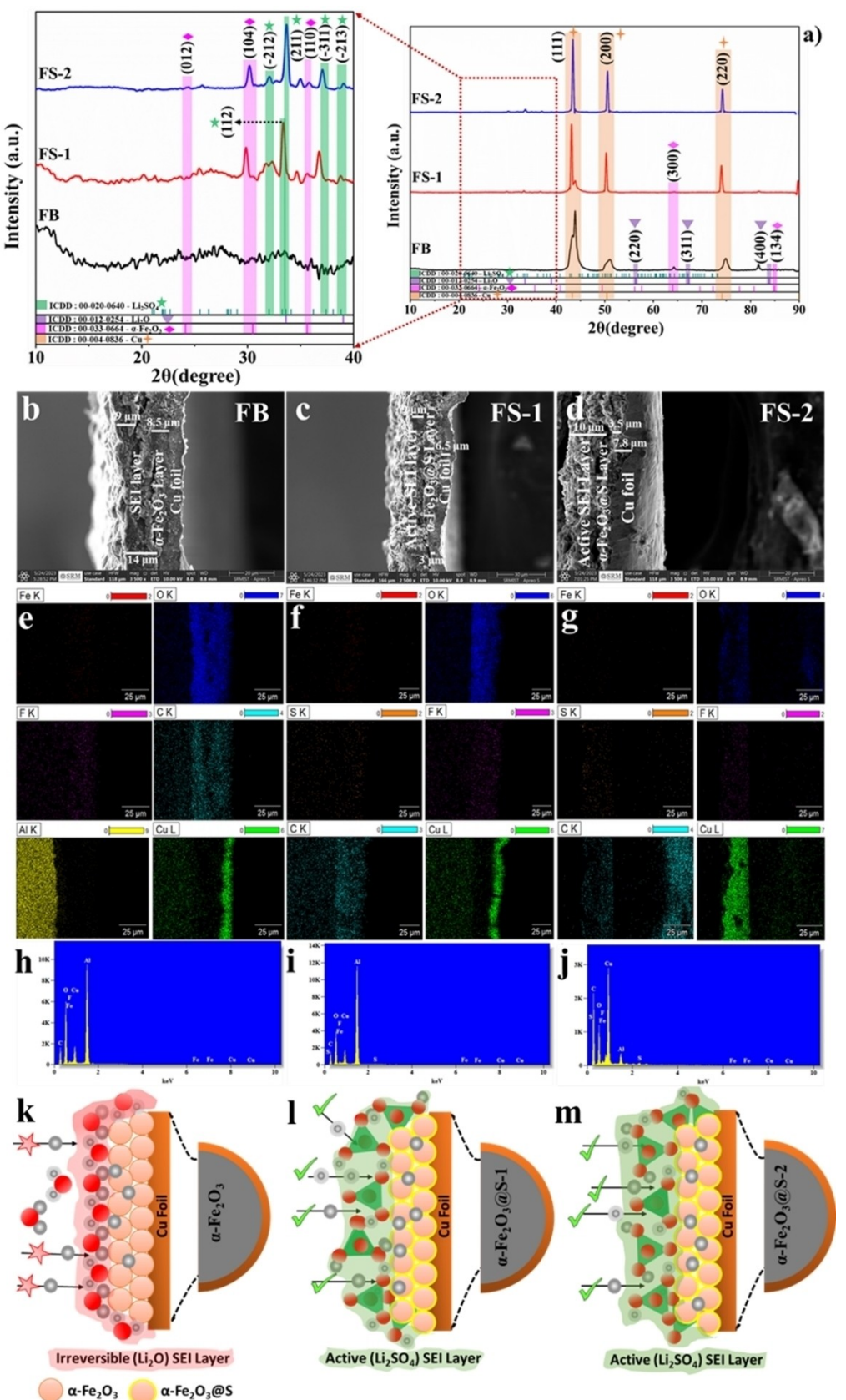


Figure 9. a) Steady mode ex-situ XRD plot of bare $\alpha\text{-Fe}_2\text{O}_3$ electrode (FB), sulfur-coated $\alpha\text{-Fe}_2\text{O}_3\text{@S-1}$ electrode (FS-1) and $\text{Fe}_2\text{O}_3\text{@S-2}$ (FS-2) working electrode after single discharge cycle vs Li^+/Li along with magnifying spectra. HR-SEM cross-section morphology of dismantled electrodes performed after a single discharge cycle b) FB, c) FS-1, and d) FS-2. e–g) cross-section elemental mapping illustrates the even distribution of elements such as Fe, O, S, F, C, Cu, and Al after a single discharge electrode, h–j) Energy Dispersive X-ray spectra (EDX) of the bare and sulfur-coated $\alpha\text{-Fe}_2\text{O}_3$ electrode, Schematic representation of (k) Passive irreversible SEI layer formation on the $\alpha\text{-Fe}_2\text{O}_3$ electrode surface, and l–m) Active Li_2SO_4 based SEI layer formation on the surface of sulfur coated $\alpha\text{-Fe}_2\text{O}_3$ (FS-1,2) electrodes.

the cross-section images are shown in Figure 9(c and d) clearly illustrate the formation of a thick SEI layer on the surface of both sulfur-coated electrodes which might be composed of Li_2SO_4 , as discussed in XRD investigations. To further characterize the components of the SEI layer, an EDX elemental mapping study has been carried out throughout the cross-section region and the results are shown in Figure 9(e-g). The EDX results indicate the homogeneous distribution of critical elements such as iron and oxygen, confirming the presence of a bare $\alpha\text{-Fe}_2\text{O}_3$ layer that aligns with the XRD findings. As shown in Figure 9(h), the EDX spectrum of FB electrode accurately reflects the presence and spread of elements such as Fe, O, C, F, Cu, and Al which are found to be consistent with the elemental mapping. Figure 9(f) shows the elemental mapping of the FS-1 electrode in the cross-section region, revealing the distribution of elements such as Fe, O, S, F, C, and Cu. The significant content of Fe and O in the sample region confirms the presence of the $\alpha\text{-Fe}_2\text{O}_3$ layer in the FS-1 electrode. Notably, sulfur is observed to be distributed from the surface of $\alpha\text{-Fe}_2\text{O}_3$ to the upper surface of SEI layer, indicating the formation of amorphous Li_2SO_4 at the electrode-electrolyte interface which might be developed during the initial discharge processes as evidenced from the ex-situ XRD. The EDX spectrum (Figure 9i) highlights the rich content of primary elements. Figure 9(g) shows elemental mapping of the FS-2 electrode, indicating the even distribution of S, Fe, and O elements in the cross-section SEM image. The uniform spread of sulfur and oxygen in the sample region extending to the top SEI layer suggests the formation of the Li_2SO_4 SEI layer, as discussed in the post-XRD analysis. Figure 9(j) depicts the EDX spectrum of the FS-2 electrode, confirming the substantial content of active elements S, Fe, and O. The elemental mapping EDX spectra of all the electrodes indicate the presence of C, F, and Cu elements which can be attributed to the carbon black used in electrode fabrication as conductive agent, PVDF based binder used in the preparation of the electrode slurry, and the copper current collector, respectively. In addition, the appearance of 'Al' might be due to the aluminium HR-SEM stub. The elemental mapping of singly discharged FS-1 and FS-2 electrodes reveals the presence of sulfur compounds in the sample and the SEI layer, confirming the inherent existence of sulfur coating in the sample and depicting the formation of lithium inter-metallic compounds involving sulfur in the SEI region, as discussed in ex-situ XRD investigations. Based on the cumulative experimental evidence and considering the facile bonding possibilities of the sulfur anion with Li^+ cations and oxygen, it's confirmed that surface sulfur participates in network bond formation with, O, and Li by forming a Li_2SO_4 based SEI layer on the surface of the FS-1 and FS-2 electrodes. The ex-situ investigations indicate that there might be a strong tendency for further development of an active Li_2SO_4 based stable protective SEI layer at the electrode-electrolyte interface upon prolonged cycles for the FS-1 and FS-2 working electrodes. This sulfur-based SEI layer effectively facilitates Li^+ ion migration and mitigates the accumulation of inactive Li_2O layers at the interface. Figure 9(k) shows a schematic representation of undesirable SEI barrier formation in $\alpha\text{-Fe}_2\text{O}_3$ electrode that hinders the lithium-ion migration where-

as the Figure 9(l-m) illustrates facile lithium-ion migration through active Li_2SO_4 SEI layer in the case of FS-1&2 electrodes. The ex-situ investigations validate the formation of an active SEI layer, which could explain the reasons behind the low initial capacity fading (ICF), high coulombic efficiency, and high energy density observed in the FS-2 electrode. Among the above studied electrodes, FS-2 ($\alpha\text{-Fe}_2\text{O}_3@\text{S-2}$) electrode has demonstrated excellent lithium-ion storage performance, and with this motivation, further efforts have been made to investigate the performance of the sulfur-coated $\alpha\text{-Fe}_2\text{O}_3$ (FS-2) electrode in Lithium-Sulfur Batteries (LiSB).

Several Researchers are currently addressing various challenges corresponding to electrode-electrolytes used in Lithium-Sulfur batteries (LiSB).^[83-87] One major issue during the discharge process is the formation of lithium polysulfides (Li_2S_x $4 \leq x \leq 8$).^[84] These polysulfides dissolve into the electrolyte and migrate towards the lithium metal anode, leading to an irreversible reaction that results the formation of Li_2S .^[85] These issues such as less utilization of sulfur and sulfur-derived products due to their non-conductive nature, as well as the capacity fading caused by Li_2S_x shuttle effect, which reduce the Coulombic efficiency of LiSB. To overcome these challenges, researchers are exploring modified sulfur electrodes coated with various materials, including metal oxides, metal sulfides and carbon-based materials.^[86,87]

These coating techniques increases the electronic conductivity of the electrode and help mitigate the dissolution of Li_2S_x in LiSB. In this scenario, the $\alpha\text{-Fe}_2\text{O}_3@\text{S-2}$ electrode, may be suitable for the LiSB based on its promising electrochemical performance in LIB. The CV measurements have been conducted for LiSB equipped with $\alpha\text{-Fe}_2\text{O}_3@\text{S-2}$ electrode at a scan rate of 0.1 mVs^{-1} . Figure 10(a) illustrates the CV results of the $\alpha\text{-Fe}_2\text{O}_3@\text{S-2}$ electrode, showing the kinetics of Li^+ in the sulfur-coated $\alpha\text{-Fe}_2\text{O}_3@\text{S-2}$ electrode within the potential window of 1.7 to 2.8 V versus Li^+/Li for the initial five cycles. The CV curves of $\alpha\text{-Fe}_2\text{O}_3@\text{S-2}$ electrode indicate a strong cathodic peak, corresponding to the reduction of $\text{S}_8/\text{Li}_2\text{S}_8$ leading to long-chain soluble lithium polysulfide shuttle and followed by short-chain insoluble Li_2S_2 and Li_2S (LiPSs). During the charging processes, multiple anodic peaks are observed, which indicates the conversion of Li_2S to S. In the discharge processes, a strong cathodic peak appears at 2.0 V, corresponding to insoluble Li_2S_2 formation, and the substantial deep discharge peak at 1.7 V corresponds to the formation of Li_2S . During the oxidation process, a small sharp peak observed at 1.8 V might be due to the oxidation of sulfur-coated $\alpha\text{-Fe}_2\text{O}_3$. In addition, there are multiple oxidation peaks observed at 2.1, 2.2, and 2.29 V, which are associated with the formation of reversible $\text{Li}_2\text{S}/\text{Li}_2\text{S}_2$ and during the reduction processes the $\text{Li}_2\text{S}/\text{Li}_2\text{S}_2$ which is reduced to S. Further cycles indicate consistency of the redox peaks, but the oxidation peak gets shifted towards the higher potential at the 5th cycle, revealing that the $\alpha\text{-Fe}_2\text{O}_3@\text{S-2}$ electrode has the minimum polarization resistance and the enhanced electrochemical reversibility. The redox peaks overlap with each other, resulting in the excellent stability of the $\alpha\text{-Fe}_2\text{O}_3@\text{S-2}$ electrode versus the electrolyte. Figure 10(b), illustrates the CV curves of the $\alpha\text{-Fe}_2\text{O}_3@\text{S-2}$ electrode at various sweep rates from 0.1 to

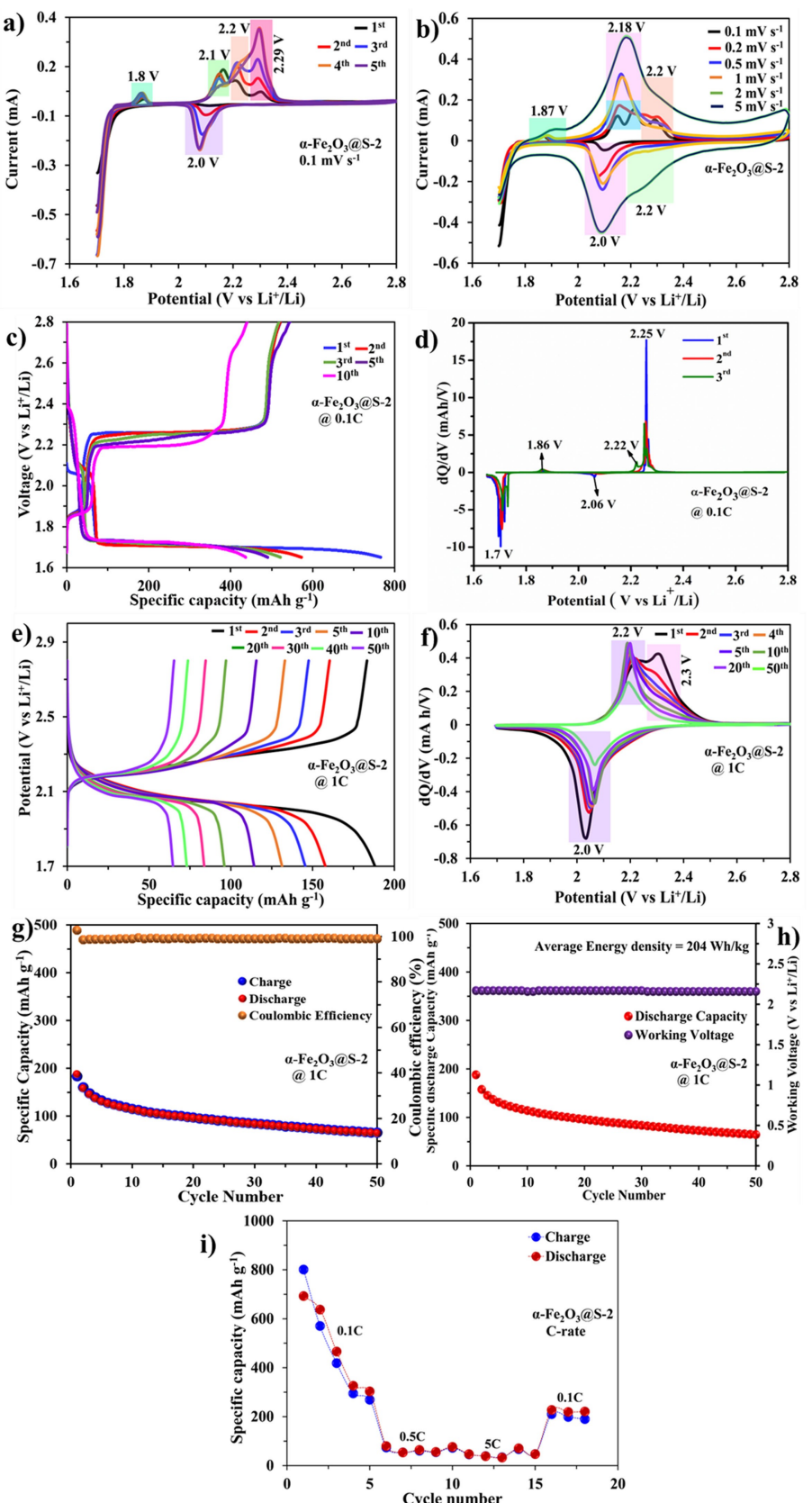


Figure 10. Electrochemical performance of as-synthesized $\alpha\text{-Fe}_2\text{O}_3@\text{S-2}$ electrode for lithium-sulfur batteries. a) CV curves of $\alpha\text{-Fe}_2\text{O}_3@\text{S-2}$ electrode in the potential range of 1.7 to 2.8 V at 0.1 mV s^{-1} . b) CV curve of $\alpha\text{-Fe}_2\text{O}_3@\text{S-2}$ electrode at various sweep rates, 0.1 to 5 mV s^{-1} . c) Galvanostatic charge-discharge of $\alpha\text{-Fe}_2\text{O}_3@\text{S-2}$ electrode for selected cycles in LiSB at 0.1 C-rate . d) dQ/dV curves of $\alpha\text{-Fe}_2\text{O}_3@\text{S-2}$ electrode at 0.1 C-rate . e) GCD curves of $\alpha\text{-Fe}_2\text{O}_3@\text{S-2}$ electrode in LiSB at 1 C-rate . f) dQ/dV curves of $\alpha\text{-Fe}_2\text{O}_3@\text{S-2}$ electrode at 1 C-rate . g) Cycling life of the LiSB based on $\alpha\text{-Fe}_2\text{O}_3@\text{S-2}$ electrode for 50 cycles. h) Cycle number vs. specific capacity of $\alpha\text{-Fe}_2\text{O}_3@\text{S-2}$ electrode with average energy density. i) C-rate capability of $\alpha\text{-Fe}_2\text{O}_3@\text{S-2}$ electrode for Li-S batteries at with various current densities.

5 mVs⁻¹ which exhibits a couple of redox peaks. A typical couple of cathodic peaks are observed at 2.2 V and 2.0 V, corresponding to the reduction from solid S₈ to high-order polysulfides ($Li_2S_8 \rightarrow Li_2S_6 \rightarrow Li_2S_4$) and then to low-order polysulfides ($Li_2S_4 \rightarrow Li_2S_2 \rightarrow Li_2S$) which is then converted into solid lithium sulfides (Li₂S/Li₂S₂).^[88] The couple of anodic peaks at 2.18 and 2.2 V result in the oxidation of solid Li₂S₂/Li₂S to lithium polysulfides (LiPS)/Sulfur. Although these processes reasonably occur, there are possibilities for an efficient conversion of S₈ to Li₂S and LiPs/sulfur. The peak current of the redox increases at higher sweep rates in-line with the square root of the scan rate which indicates good redox repeatability, retention and superiority of the α -Fe₂O₃@S-2 electrode for LiSB. This trend and the increasing redox peak current at higher scan rates suggest excellent electrochemical stability and reversibility of the α -Fe₂O₃@S-2 electrode for Li-S batteries.

Figure 10(c) shows the charge-discharge profile of α -Fe₂O₃@S-2 electrode in LiS cell vs Li⁺/Li in the potential window of 1.65 to 2.8 V at 0.1 C-rate. The initial discharge-charge capacity of α -Fe₂O₃@S-2 for first cycle is observed as 766, 520 mAh g⁻¹, respectively while that of second cycle is found to be 572, and 520 mAh g⁻¹, respectively. Upon further redox cycles, there is no drastic capacity fading observed which indicates an excellent redox stability of the electrode. During the discharge process, capacity corresponding to the high-voltage plateau (2.4 to 2.1 V) indicates the reduction processes from elemental sulfur to soluble polysulfides (Li₂S_n, 4 < n < 8), and the capacity estimated for the well defined low-voltage plateau (2.1 to 1.7 V) represents continuing reduction at the cathode from soluble polysulfide to insoluble sulfide (Li₂S₄ to LiS). The high voltage plateau is associated with the formation of soluble polysulfides which may be resulted in polysulfide diffusion.

Figure 10(d) shows the dQ/dV graph of α -Fe₂O₃@S-2 electrode Vs Li⁺/Li at 0.1 C-rate in the potential window of about 1.65 to 2.8 V. The dQ/dV plot results show typical cathodic peaks at 2.06 V and a strong sharp peak at 1.7 V^[89,90] which are corresponding to the reduction from solid S₈ to high-order polysulfides ($Li_2S_8 \rightarrow Li_2S_6 \rightarrow Li_2S_4$) and then to low-order polysulfides ($Li_2S_4 \rightarrow Li_2S_2 \rightarrow Li_2S$). Subsequently, couple of anodic peaks are observed at 1.86, 2.22 and 2.25 V resulted in the oxidation of solid Li₂S to lithium polysulfides (LiPS)/Sulfur (i.e., Li₂S₈/S₈).

Notably, the overlapped peaks about 2.15 and 2.36 V confirm the efficient conversion of S₈ to Li₂S and LiPS/Sulfur. A smaller overpotential indicates the enhanced electrochemical performance of α -Fe₂O₃@S-2 in LiSB. The electrochemical utilization of the sulfur and the improved cyclability is revealed by the GCD results. Figure 10(e) illustrates the GCD profile of α -Fe₂O₃@S-2 versus Li⁺/Li at a current rate of 1 C. The GCD curves exhibit the initial discharge capacity observed at 188 mAh g⁻¹ and the charge capacity of 183 mAh g⁻¹, respectively. The second cycle exhibits the charge-discharge capacity of 160 and 157 mAh g⁻¹, respectively. The GCD plateaus proved a detailed analysis of several key characteristics necessary for understanding electrode kinetics. Examining the voltage profile, the discharge curves clearly show the multi-stage sulfur reduction to

Li₂S as it accepts lithium-ions and electrons which is evident from the plateaus observed in high and low-voltage regions. Upon further cycling, charge-discharge capacity fading is observed which might be due to the fast lithium-ion kinetics in the α -Fe₂O₃@S-2 electrode at 1 C-rate. The voltage polarization (ΔV) upon effective sulfur utilization during the charge-discharge cycle is $\Delta V = 0.147$ at 1 C-rate for the α -Fe₂O₃@S-2 electrode. Such a minimal ' ΔV ' implies lower resistance of α -Fe₂O₃@S-2 electrode that enhances diffusion of Li⁺-ions into the electrode particles and also offers an efficient ionic conduction across the sulfur-coated α -Fe₂O₃@S-2 working electrode. A series of chemical transformations may be possible due to the lower ion transport resistance in the α -Fe₂O₃@S-2 electrode such as solid-state sulfur (S₈) to liquid-state sulfur (S₄²⁻) followed by insoluble sulfides (Li₂S), giving rise to an additional capacity. Figure 10(f) shows the dQ/dV curves corresponding to the α -Fe₂O₃@S-2 electrode GCD at 1 C-rate which indicates the redox kinetics of α -Fe₂O₃@S-2 electrode. The dQ/dV results of the sulfur-coated α -Fe₂O₃@S-2 electrode indicate the typical reduction and oxidation characteristics which might be responsible for the reduction of (S₈) to higher-order polysulfides (Li₂S₄) and then to low-order polysulfides (Li₂S). The typical strong cathodic peak observed at 2.0 V corresponds to the reduction from solid S₈ → Li₂S. Subsequently, the anodic scan converts as formed Li₂S/Li₂S₂ to lithium polysulfides (LiPS)/sulfur which is corresponding to the overlapped peaks observed about 2.2 and 2.3 V. This result confirms the conversion of S₈ to Li₂S and LiPS/Sulfur. Figure 10(g) shows long-cyclic life of α -Fe₂O₃@S-2 electrode as validated through the GCD cycling studies at the current rate of 1 C. The initial discharge process is delivering a discharge capacity of 188 mAh g⁻¹ which fades down to 64 mAh g⁻¹ at the end of the 50th cycle. The charge-discharge capacity fading is due to the fast lithium kinetics, and LiPSs at the α -Fe₂O₃@S-2 electrode. Figure 10(h) illustrates the specific discharge capacity and working potential versus cycle number. The initial working potential of the α -Fe₂O₃@S-2 electrode in LiSB is found to be 2.17 V whereas at end of the 50th cycle, and the working potential is almost stable around 2.16 V which yields the average energy density of 204 Wh/kg. Figure 10(i) illustrates the C-rate performance of sulfur-coated α -Fe₂O₃@S-2 electrode Vs Li⁺/Li at various current densities. As the current density increases, a descending step-like behaviour in specific discharge capacity is observed. The initial discharge of the α -Fe₂O₃@S-2 electrode delivers 801 mAh g⁻¹ at 0.1 C-rate, which drops to 79 mAh g⁻¹ at 5 C-rate. When the current density gradually decreases from 5 C to 0.1 C-rate, the α -Fe₂O₃@S-2 electrode partially gains back a discharge capacity of 227 mAh g⁻¹ at 0.1 C-rate, which includes initial drastic capacity fading. In order to understand the internal cell resistance of the LiSB, a detailed EIS analysis of the α -Fe₂O₃@S-2 electrode before and after cycle is exemplified in Supplementary Information (Figure S7). The increase in cell resistance after prolonged cycles indicate a pile-up of sulfur coating on the electrode that decreases the capacity down to 64 mAh g⁻¹ at 50th cycle. However, the capacity fading is not drastic due to the protective sulfur coated layer on the electrode surface and the electrode with stand

even at high C rate and long cycles. This highlights the excellent electrochemical performance of the $\alpha\text{-Fe}_2\text{O}_3@\text{S-2}$ electrode for lithium-sulfur batteries.

The overall electrochemical performance of $\alpha\text{-Fe}_2\text{O}_3@\text{S-2}$ electrode is excellent in LIB as well as LISB. As evidenced from ex-situ analyses, the in-situ formed electrochemically induced active Li_2SO_4 SEI layer played a significant role increasing the electrochemical performance of LIB cells. Significantly, this active SEI layer alleviates the formation of undesirable lithium inter-metallic SEI layer formation through capturing of surface adsorbed oxygen molecules in the form of Li_2SO_4 . Interestingly, this Li_2SO_4 based SEI layer is ion conductive and acts as a protective layer on the electrode surface that prevents direct contact between electrode-electrolyte which not only shielding the electrode from vulnerable surface reactions but also safeguard the electrolyte from decomposition within the potential window. Figure S(8) shows digital images of the blue LEDs powered-up by using LIB coin cells equipped with bare and sulfur coated $\alpha\text{-Fe}_2\text{O}_3$ electrodes and also by using LISB coin cell with $\alpha\text{-Fe}_2\text{O}_3@\text{S-2}$ electrode. The blue LED lighting test indicates relatively good powering stamina of LIB coin cell with $\alpha\text{-Fe}_2\text{O}_3@\text{S-2}$ electrode which might be due to the Li_2SO_4 active layer as evidenced from detailed ex-situ investigations. In addition, the presence of oxygen defects in $\alpha\text{-Fe}_2\text{O}_3$ host also contribute expedite lithium-ion kinetics as evidenced by HR-TEM, XPS and charge-discharge results. The cumulative synergistic performance of sulfur coating by microwave assisted method in the $\alpha\text{-Fe}_2\text{O}_3@\text{S-2}$ electrode excels in exhibiting excellent cyclic, C-rate capability and LED powering endurance in LIB as well as LISB. In nutshell, the sulfur coating proves an excellent volume controller for $\alpha\text{-Fe}_2\text{O}_3$ based anodes during redox reactions; facilitates lithium-ion mobility across the nanoparticles, and also effectively protects the electrode surface from vulnerable inactive SEI barrier developments.

Conclusions

In this article, the merits of sulfur coating on $\alpha\text{-Fe}_2\text{O}_3$ nanosheet and its significance to the performance of redox kinetics have been discussed in detail. The ferric oxide-based compounds such as bare $\alpha\text{-Fe}_2\text{O}_3$, sulfur coated $\alpha\text{-Fe}_2\text{O}_3@\text{S-1}$, and $\alpha\text{-Fe}_2\text{O}_3@\text{S-2}$ nanosheets as anode material for LiB have been synthesized by pechini method. HRSEM morphological analysis confirms the nanosheet formation of bare and sulfur-coated $\alpha\text{-Fe}_2\text{O}_3$ powdered samples. The HR-TEM morphological investigation of $\alpha\text{-Fe}_2\text{O}_3@\text{S-1}$ and $\alpha\text{-Fe}_2\text{O}_3@\text{S-2}$ powdered samples reveals the nanosheet formation and additionally with a fine, elegant sulfur coating on $\alpha\text{-Fe}_2\text{O}_3$, with a thickness of about ~ 9 nm for $\alpha\text{-Fe}_2\text{O}_3@\text{S-1}$ and ~ 8 nm for $\alpha\text{-Fe}_2\text{O}_3@\text{S-2}$ powdered samples. The SAED pattern of as-synthesized $\alpha\text{-Fe}_2\text{O}_3@\text{S-1}$ and $\alpha\text{-Fe}_2\text{O}_3@\text{S-2}$ powdered samples confirms the formation of two distinct polycrystalline structures corresponding to the surface coating of sulfur and core $\alpha\text{-Fe}_2\text{O}_3$ nanosheet. XPS analysis indicates a dominant Fe^{3+} oxidation state corresponding to the $\alpha\text{-Fe}_2\text{O}_3$ for all the samples. The cyclic voltammogram results of sulfur-coated $\alpha\text{-Fe}_2\text{O}_3@\text{S-2}$ electrode indicate well-defined redox

peaks overlapped with one another, which reveals excellent reversibility. The CV result of the $\alpha\text{-Fe}_2\text{O}_3@\text{S-2}$ electrode further confirms the formation of Li_2SO_4 based active SEI layer formation that alleviates the usual Li_2O -based passive SEI layer formation. The GCD results exhibit the initial charge-discharge capacities for bare- $\alpha\text{-Fe}_2\text{O}_3$, $\alpha\text{-Fe}_2\text{O}_3@\text{S-1}$, and $\alpha\text{-Fe}_2\text{O}_3@\text{S-2}$ electrodes as $946\text{--}467 \text{ mAh g}^{-1}$, $1051\text{--}598 \text{ mAh g}^{-1}$ and $1194\text{--}871 \text{ mAh g}^{-1}$, respectively. The cycling stability of sulfur-coated $\alpha\text{-Fe}_2\text{O}_3@\text{S-2}$ electrode delivers excellent electrochemical stability until 500 cycles with a discharge capacity of 76 mAh g^{-1} as well as 100% coulombic efficiency, which is relatively better than that of the bare- $\alpha\text{-Fe}_2\text{O}_3$ electrode. The $\alpha\text{-Fe}_2\text{O}_3@\text{S-2}$ electrode exhibits high lithium-ion diffusion kinetics electrode delivers relatively high in the order of 10^{-11} to $10^{-10} \text{ cm}^2 \text{ s}^{-1}$, which might be due to the alleviation of passive SEI layer formation. The $\alpha\text{-Fe}_2\text{O}_3@\text{S-2}$ electrode delivers a discharge capacity of about 225 mAh g^{-1} at a 2 C-rate, resulting in an excellent electrochemical performance even at a high C-rate, which might be due to the formation of the SEI layer and its high lithium-ion kinetics. The sulfur coating protects the $\alpha\text{-Fe}_2\text{O}_3$ nanosheet from electrode structure deterioration and fracture of the electrode particle that, alleviates the initial drastic capacity fading. Compared to all the electrodes, the $\alpha\text{-Fe}_2\text{O}_3@\text{S-2}$ delivers a high energy density of about $\sim 246 \text{ Wh/kg}$ even after 100 cycles and $\sim 97 \text{ Wh/kg}$ after 500 cycles at 1 C rate, respectively. An in-depth ex-situ XRD, cross-section HR-SEM investigations on single discharged sulfur-coated electrodes $\alpha\text{-Fe}_2\text{O}_3@\text{S-1}$ and $\alpha\text{-Fe}_2\text{O}_3@\text{S-2}$ confirms the formation of the Li_2SO_4 SEI layer on the surface of the electrode. This Li_2SO_4 based active layer contributes to the efficient Li^+ ion migration across the interface of electrode-electrolyte interface. The outperformed $\alpha\text{-Fe}_2\text{O}_3@\text{S-2}$ electrode material has also been used to fabricate a Lithium-sulfur battery. The Li-S device exhibits excellent charge-discharge specific capacity of 650 mAh g^{-1} and 477 mAh g^{-1} in the first cycle at 0.1 C-rate, respectively. The optimal energy density of the $\alpha\text{-Fe}_2\text{O}_3@\text{S-2}$ with Li-S is $\sim 204 \text{ Wh/kg}$ after the 50th cycle at 1 C-rate, respectively. The sulfur-coated core-shell structured $\alpha\text{-Fe}_2\text{O}_3$ nanosheet electrode treated by microwave-assisted technique is found to be highly suitable for LIB and LISB applications. The electrochemical and ex-situ investigation results indicate interesting electrochemically induced reaction kinetics for the formation of Li_2SO_4 based active SEI layer that plays a vital role in alleviating vulnerable Li_2O -based SEI formation as well as indirectly contributing in reducing the electrolyte decomposition. Furthermore, the Li_2SO_4 based active layer effectively protects the electrode surface and providing facile Li^+ ion diffusion pathways that enhance the redox kinetics. The $\alpha\text{-Fe}_2\text{O}_3@\text{S-2}$ electrode exhibits outstanding performance in cycling, C-rate, and endurance in blue LED lighting. These interesting findings suggest that the usage of sulfur in the form of an additive/coating element for the negative as well as positive electrodes may contribute significantly to alleviate the vulnerable SEI as well as cathode electrolyte interface (CEI) layer formations.

Acknowledgements

This research work has been received financial support from the Department of Science and Technology-Science and Engineering Research Board (DST-SERB), New Delhi, India (File No: ECR/2017/000095/ES). The authors wish to express their immense gratitude to Mr. Vadivel, Senior Scientific Officer and Mr. Prakatheswaran, Junior Scientific Officer for their support in HR-TEM measurements. The authors thank Mr. Asswin, and Mr. Kubenthirapandian, Junior Scientific Officer, SRM Central Instrumental Facility (SCIF), SRMIST for their assistance in HR-SEM measurements. The author appreciate the Department of Chemistry, SRMIST for rendering support in performing Ex-situ XRD measurements. The authors extend their heartfelt thanks to Dr. Raghu Subash Chandrabose and Mr. Narayananakumar (G-Power Energy & Technology, and Hydrographenium Indus pvt Ltd.) for their valuable assistance with the CR 2032-coin cell components.

Conflict of Interests

The authors declare no conflict of interest.

Data Availability Statement

The data that support the findings of this study are available from the corresponding author upon reasonable request.

Keywords: $\alpha\text{-Fe}_2\text{O}_3$ nanosheet • Interfacial mechanism • oxygen defects • Anionic-derived Li_2SO_4 • active interfacial layer • Li-ion storage

- [1] J. E. N. Swallow, M. W. Fraser, N.-J. H. Kneusels, J. F. Charlton, C. G. Sole, C. M. E. Phelan, E. Björklund, P. Bencok, C. Escudero, V. Pérez-Dieste, *Nat. Commun.* **2022**, *13*, 6070.
- [2] S. E. Bak, W. Chung, M. A. Abbas, J. H. Bang, *ACS Appl. Mater. Interfaces* **2023**, *15*, 34874.
- [3] J. Islam, F. I. Chowdhury, J. Uddin, R. Amin, J. Uddin, *RSC Adv.* **2021**, *11*, 5958.
- [4] G. Wang, M. Aubin, A. Mehta, H. Tian, J. Chang, A. Kushima, Y. Sohn, Y. Yang, *Adv. Mater.* **2020**, *32*, 2003684.
- [5] C. Huang, J. Mahmood, Z. Wei, D. Wang, S. Liu, Y. Zhao, H. J. Noh, J. Ma, J. Xu, J. B. Baek, *Mater. Today* **2019**, *14*, 100359.
- [6] L. Sun, Y. Liu, R. Shao, J. Wu, R. Jiang, Z. Jin, *Energy Storage Mater.* **2022**, *46*, 482.
- [7] Q. Gan, B. Wu, N. Qin, J. Chen, W. Luo, D. Xiao, J. Feng, W. Liu, Y. Zhu, P. Zhang, *Electrochim. Acta* **2020**, *343*, 136121.
- [8] Q. Hao, J. Wang, C. Xu, *J. Mater. Chem. A* **2014**, *2*, 87.
- [9] S. Yun, Y. C. Lee, H. S. Park, *Sci. Rep.* **2016**, *6*, 1.
- [10] M. V. Reddy, T. Yu, C. H. Sow, Z. X. Shen, C. T. Lim, G. V. S. Rao, B. V. R. Chowdari, *Adv. Funct. Mater.* **2007**, *17*, 2792.
- [11] J. Wu, P. Zhang, X. Chen, Y. Wang, Q. Zhang, S. Yu, M. Wu, *ChemElectroChem* **2022**, *9*, 2.
- [12] Y. Fu, H. Zhou, Z. Hu, S. Yin, L. Zhou, *Compos. Commun.* **2020**, *22*, 100446.
- [13] Y. Wang, L. Cao, J. Li, L. Kou, J. Huang, Y. Feng, S. Chen, *Chem. Eng. J.* **2020**, *391*, 123597.
- [14] F. Zhou, L. Zeng, W. Guo, Y. Yan, F. Wu, M. Pan, *Int. J. Energy Res.* **2019**, *43*, 7095.
- [15] J. Wang, C. Ma, J. Tang, X. Yang, Y. Wang, X. Jia, W. Cai, W. Qiao, L. Ling, *Energy Fuels* **2021**, *35*, 816.
- [16] W. Zhu, Y. Wang, Y. Yu, Y. Hu, Y. Chen, *J. Alloys Compd.* **2020**, *813*, 152175.
- [17] H. Zhu, Q. Wei, S. Yu, P. Guo, J. Li, Y. Wang, *J. Electron. Mater.* **2022**, *51*, 4207.
- [18] S. S. Li, W. J. Li, T. J. Jiang, Z. G. Liu, X. Chen, H. P. Cong, J. H. Liu, Y. Y. Huang, L. N. Li, X. J. Huang, *Anal. Chem.* **2016**, *88*, 906–914.
- [19] M. S. Hossain, T. Furusawa, M. Sato, *Adv. Powder Technol.* **2022**, *33*, 103797.
- [20] E. Anastasiou, K. O. Lorentz, G. J. Stein, P. D. Mitchell, *Lancet Infect. Dis.* **2014**, *14*, 553.
- [21] Y. S. Choi, W. Choi, W. S. Yoon, J. M. Kim, *ACS Nano* **2022**, *16*, 631.
- [22] Q. Ban, Y. Liu, P. Liu, Y. Li, Y. Qin, Y. Zheng, *Microporous Mesoporous Mater.* **2022**, *335*, 111803.
- [23] S. Yu, X. He, Z. Zhu, T. Chen, L. Xiao, H. Sui, K. Hu, Y. Wei, C. Li, H. Zhu, Z. Xiao, *J. Electroanal. Chem.* **2023**, *943*, 117624.
- [24] S. Chamola, S. Ahmad, *Adv. Sustainable Syst.* **2023**, *7*, 1.
- [25] M. Zheng, H. Tang, L. Li, Q. Hu, L. Zhang, H. Xue, H. Pang, *Adv. Sci.* **2018**, *5*, 1700592.
- [26] M. Valvo, C. Floraki, E. Paillard, K. Edström, D. Vernardou, *Nanomaterials* **2022**, *12*, 1.
- [27] Y. Yang, X. Fan, G. Casillas, Z. Peng, G. Ruan, G. Wang, M. J. Yacaman, J. M. Tour, *ACS Nano* **2014**, *8*, 3939.
- [28] C. Li, Y. Lin, X. Li, Z. Li, P. Luo, Y. Jin, Z. Li, *Colloids Surf. A* **2023**, *660*, 130681.
- [29] B. Konkena, H. Kaur, R. Tian, C. Gabbett, M. McCrann, D. V. Horvath, K. Synnatschke, A. Roy, R. Smith, V. Nicolosi, M. D. Scanlon, J. N. Coleman, *Small* **2022**, *18*, 2203918.
- [30] T. Zhang, J. Zheng, Z. Liang, B. Zhao, H. Zeng, W. Guo, L. Zhao, Y. Sun, I. Abdulhalim, L. Jiang, *Electrochim. Acta* **2019**, *306*, 151.
- [31] T. Chen, W. Jiang, X. Sun, W. Ning, Y. Liu, G. Xu, G. Han, *ChemistrySelect* **2020**, *5*, 430.
- [32] H. Li, L. J. Wu, S. G. Zhang, C. Yao, C. Y. Chao, H. W. Yue, H. H. Fan, *J. Alloys Compd.* **2020**, *832*, 155008.
- [33] Q. Shi, Y. Zhou, J. Cheng, Y. Pan, Y. Wu, L. Zhu, Z. Yuan, *Microporous Mesoporous Mater.* **2022**, *332*, 111681.
- [34] F. Dou, L. Shi, G. Chen, D. Zhang, *Silicon/Carbon Composite Anode Materials for Lithium-Ion Batteries*, Springer Singapore, **2019**.
- [35] Z. Yan, Z. Sun, A. Li, H. Liu, Z. Guo, L. Qian, *Adv. Compos. Hybrid Mater.* **2021**, *4*, 716.
- [36] Y. Wang, P. Mao, F. Yan, C. Gao, Y. Liu, J. Ding, W. Wu, Y. Liu, *Synth. Met.* **2016**, *222*, 198.
- [37] M. Jalili, H. Ghanbari, R. Malekfar, S. S. Mousavi Masouleh, *ACS Omega* **2020**, *5*, 3563.
- [38] R. Zhang, Y. Fang, T. Chen, F. Qu, Z. Liu, G. Du, A. M. Asiri, T. Gao, X. Sun, *ACS Sustainable Chem. Eng.* **2017**, *5*, 7502.
- [39] Y.-S. Su, A. Manthiram, *Electrochim. Acta* **2012**, *77*, 272.
- [40] Y. S. Su, Y. Fu, A. Manthiram, *Phys. Chem. Chem. Phys.* **2012**, *14*, 14495.
- [41] Y. Bai, J. Yeom, M. Yang, S. H. Cha, K. Sun, N. A. Kotov, *J. Phys. Chem. C* **2013**, *117*, 2567.
- [42] X. Yan, Y. Wu, D. Li, J. Hu, G. Li, P. Li, H. Jiang, W. Zhang, *J. Mater. Sci.* **2018**, *53*, 15850.
- [43] B. Lv, H. Zhou, D. Wu, Y. Xu, *J. Nanopart. Res.* **2014**, *16*, 2799.
- [44] X. Liu, W. Si, J. Zhang, X. Sun, J. Deng, S. Baunack, S. Oswald, L. Liu, C. Yan, O. G. Schmidt, *Sci. Rep.* **2014**, *4*, 1.
- [45] S. Tian, Y. Yin, Z. Cao, H. Yue, S. Yang, *Ionics* **2018**, *24*, 33.
- [46] X. Zhang, Y. Niu, Y. Li, X. Hou, Y. Wang, R. Bai, J. Zhao, *Mater. Lett.* **2013**, *99*, 111.
- [47] M. Chen, E. Zhao, Q. Yan, Z. Hu, X. Xiao, D. Chen, *Sci. Rep.* **2016**, *6*, 1.
- [48] L. T. Quispe, L. G. L. Mamani, A. A. Baldárrago-Alcántara, L. L. Félix, G. F. Goya, J. A. Fuentes-García, D. G. Pacheco-Salazar, J. A. H. Coaquirá, *Nanotechnology* **2022**, *33*, 335704.
- [49] T. Yamashita, P. Hayes, *Appl. Surf. Sci.* **2008**, *254*, 2441.
- [50] D. K. Bora, A. Braun, S. Erat, O. Safonova, T. Graule, E. C. Constable, *Curr. Appl. Phys.* **2012**, *12*, 817.
- [51] Y. Xu, H. Zhang, D. Gong, Y. Chen, S. Xu, P. Qiu, *J. Mater. Sci.* **2022**, *57*, 19716.
- [52] K. Lv, P. Wang, C. Wang, Z. Shen, Z. Lu, H. Zhang, M. Zheng, P. He, H. Zhou, *Small* **2020**, *16*, 1.
- [53] S. Jain, J. Shah, N. S. Negi, C. Sharma, R. K. Kotnala, *Int. J. Energy Res.* **2019**, *43*, 4743.
- [54] C. Zhang, S. Liu, T. Chen, Z. Li, J. Hao, *Chem. Commun.* **2019**, *55*, 7370.
- [55] M. Alaim, M. A. Shah, *Vacuum* **2023**, *210*, 111903.
- [56] R. Demir-cakan, M. Morcrette, F. Nouar, C. Davoisne, T. Devic, D. Gonbeau, R. Dominko, C. Serre, *J. Am. Chem. Soc.* **2011**, *133*(40), 16154–16160.

- [57] J. Wang, H. Yang, C. Guan, J. Liu, Z. Chen, P. Liang, Z. Shen, *J. Mater. Chem. A* **2017**, *5*, 24602–24611.
- [58] B. Li, L. Jiang, X. Li, P. Ran, P. Zuo, A. Wang, L. Qu, Y. Zhao, *Scientific Reports* **2017**, *7*, 1182.
- [59] H. W. N. Esbitt, M. S. Caini, H. H. Öchst, G. M. B. Ancroft, A. G. S. Chaufuss, R. S. Zargan, *American Mineralogist* **1998**, *9*–*10*, 1067–1076.
- [60] J. Chen, X. Zhou, C. Mei, J. Xu, S. Zhou, C. Wong, *Electrochim. Acta* **2016**, *222*, 172–176.
- [61] Y. Gao, Z. Li, Z. Fu, H. Zhang, G. Wang, H. Zhou, *Sep. Purif. Technol.* **2021**, *262*, 118336.
- [62] J. Wang, H. He, Z. Wu, J. Liang, L. Han, H. L. Xin, X. Guo, Y. Zhu, D. Wang, *J. Power Sources* **2018**, *392*, 193.
- [63] Q. Ma, Q. Zhuang, J. Liang, Z. Zhang, J. Liu, H. Peng, *Nano materials* **2017**, *12*, 431.
- [64] W. Teng, M. Huo, Z. Sun, W. Yang, X. Zheng, *Frontiers in Chemistry* **2020**, *8*, 334.
- [65] A. Jin, M. Kim, K. Lee, S. Yu, Y. Sung, *Nano Research* **2019**, *12*, 695.
- [66] T. K. Trinh, N. Tam, N. Truong, V. Thanh, H. Pham, H. Kim, C. Park, *Korean Journal of Chemical Engineering* **2018**, *35*, 1525–1531.
- [67] A. R. Pratt, I. J. Muir, H. W. Nesbitt, *Geochimica et Cosmochimica Acta* **1994**, *58*, 827.
- [68] J. Chen, K. Zhu, Y. Rao, P. Liang, J. Zhang, H. Zheng, F. Shi, K. Yan, J. Wang, J. Liu, *Dalton Trans.* **2023**, *52*, 1919.
- [69] G. Kanimozhhi, N. Nibagani, D. S. Nair, H. Kumar, N. Satyanarayana, *J. Phys. Chem. Solids* **2022**, *169*, 110885.
- [70] Q. Kang, Y. Qin, J. Shi, B. Xiong, W. Tang, F. Gao, Q. Lu, *J. Colloid Interface Sci.* **2022**, *622*, 780.
- [71] S.-P. Guo, J.-C. Li, Z. Ma, Y. Chi, H.-G. Xue, *J. Mater. Sci.* **2017**, *52*, 2345.
- [72] L. Fei, Q. Lin, B. Yuan, G. Chen, P. Xie, Y. Li, Y. Xu, S. Deng, S. Smirnov, H. Luo, *ACS Appl. Mater. Interfaces* **2013**, *5*, 5330.
- [73] J. Yang, Q. Zhang, Z. Wang, Z. Wang, L. Kang, M. Qi, M. Chen, W. Liu, W. Gong, W. Lu, P. P. Shum, L. Wei, *Advanced Energy Materials* **2020**, *33*, 2001064.
- [74] Y. S. Lee, K. S. Ryu, *Sci. Rep.* **2017**, *7*, 16617.
- [75] X. Jin, Y. Li, J. Jiang, S. Xiao, J. Yang, J. Yao, *Ionics* **2021**, *27*, 3291.
- [76] P. Xu, K. Ye, M. Du, J. Liu, K. Cheng, J. Yin, G. Wang, D. Cao, *RSC Adv.* **2015**, *5*, 36656.
- [77] L. Xiong, S. Huang, X. Yang, M. Qiu, Z. Chen, Y. Yu, *Electrochim. Acta* **2011**, *56*, 2735.
- [78] J. Zhao, J. Sun, A. Pei, G. Zhou, K. Yan, Y. Liu, D. Lin, Y. Cui, *Energy Storage Mater.* **2018**, *10*, 275.
- [79] F. Ye, H. Noh, J. Lee, H. T. Kim, *J. Mater. Chem. A* **2018**, *6*, 6617.
- [80] K. Han, J. Shen, C. M. Hayner, H. Ye, M. C. Kung, H. H. Kung, *J. Power Sources* **2014**, *251*, 331.
- [81] J. Guo, Z. Yang, Y. Yu, H. D. Abruña, L. A. Archer, *J. Am. Chem. Soc.* **2013**, *135*, 763.
- [82] H. Yu, P. Zeng, H. Liu, X. Zhou, C. Guo, Y. Li, S. Liu, M. Chen, X. Guo, B. Chang, *ACS Appl. Mater. Interfaces* **2021**, *13*, 32968.
- [83] Y. Zhao, Z. Gu, W. Weng, D. Zhou, Z. Liu, W. Fan, S. Deng, H. He, X. Yao, *Chinese Chemical Letters* **2023**, *34*, 107232.
- [84] S. Deng, X. Shi, Y. Zhao, C. Wang, J. Wu, X. Yao, *Chem. Eng. J.* **2022**, *433*, 133683.
- [85] F. Tian, M. Chang, M. Yang, W. Xie, S. Chen, X. Yao, *Chem. Eng. J.* **2023**, *472*, 144914.
- [86] M. Yang, Y. Yao, M. Chang, F. Tian, W. Xie, X. Zhao, Y. Yu, *Advanced Energy Materials* **2023**, *28*, 2300962.
- [87] J. Wu, S. Liu, F. Han, X. Yao, C. Wang, *Advanced Materials* **2021**, *6*, 2000751.
- [88] G. Liu, Q. Sun, Q. Li, J. Zhang, J. Ming, *Energy Fuels* **2021**, *35*, 10405.
- [89] R. Fang, J. Xu, D.-W. Wang, *Energy Environ. Sci.* **2020**, *13*, 432.
- [90] S. Komaba, K. Shimomura, N. Yabuuchi, T. Ozeki, H. Yui, K. Konno, *J. Phys. Chem. C* **2011**, *115*, 13487.

Manuscript received: January 13, 2024

Revised manuscript received: March 1, 2024

Accepted manuscript online: March 14, 2024

Version of record online: April 3, 2024